
# UNIVERSITÀ DEGLI STUDI DI PADOVA

**Dipartimento di Fisica e Astronomia "Galileo Galilei"**

**Erasmus Mundus Joint Master Degree on Nuclear Physics**

**Final Dissertation**

## Lifetimes measurements in neutron-deficient $^{105}$In and $^{104}$Cd isotopes with the plunger technique

**Thesis supervisors**

**Dr. Andrea Gottardo**

**Dr. Francesco Recchia**

**Candidate**

**Wenling Dong**

**Academic Year 2019/2020**

# Acknowledgements

I would like to express my sincere gratitude to my supervisors Dr. A. Gottardo and Dr. F. Recchia for their support and arrangement for my work in this difficult time due to the novel coronavirus pandemic. Especially, I would like to express my warm thanks to Dr. A. Gottardo for his patience and valuable advices on how to deal with unexpected problems during the data analysis. Special thanks to them for their detailed review and excellent suggestions during the report writing.

Finally, I would like to thank my parents and friends for cheering me on. I couldn't have done it without you in this difficult situation.

# Abstract

In order to extend our information on absolute transition probabilities in the $^{100}$Sn region, the lifetimes of the neutron-deficient $^{105}$In, $^{104}$Cd isotopes have been investigated with the coincidence Recoil Distance Doppler Shift (RDDS) technique following the fusion evaporation reaction $^{50}$Cr + $^{58}$Ni. The identification of the reaction products was obtained on an event-by-event basis using the Si detector array EUCLIDES. In coincidence with EUCLIDES, $\gamma$ rays were detected by the GALILEO spectrometer.

The experimental method was validated by remeasuring the known lifetime of the lowest-lying states in $^{104}$Cd and $^{105}$In. The limitations of the Differential Decay Curve Method and Decay Curve Method were analytically illustrated. Five lifetimes in the ground state band (GSB) of $^{105}$In and four lifetimes in $^{104}$Cd with drastically reduced errors were deduced using the plunger technique. The results are compared with the values adopted in the literature. The lifetime of the $12^+$ state of $^{104}$Cd was measured for the first time.

In addition, the measured lifetimes enabled the assessments of the multipolarities of the $\gamma$ rays depopulating the states of interest. Information on electromagnetic transition strengths were deduced for the $\gamma$-ray transitions from the $17/2^+$ up to $25/2^+$ states in $^{105}$In. In the case of $^{104}$Cd, $B(E2)$ strengths were extracted for the lowest-lying $2^+$ and $4^+$ states and compared with earlier results of $^{102}$Cd and $^{106}$Cd to indicate the robust Z = 50 shell closure. While the $B(M1)$ strengths for the $11^+$ and $12^+$ states were deduced in order to test the possibility of magnetic rotation in this near spherical nucleus.

# Table of Contents

# List of Abbreviations

**LNL**

Laboratori Nazionali di Legnaro

**GSB**

Ground State Band

**RDDS**

Recoil Distance Doppler Shift method

**DDCM**

Differential Decay Curve Method

**DCM**

Decay Curve Method

**HPGe**

high-purity germanium

**BGO**

Bismuth Germanate

**PID**

Particle Identity

# Chapter 1

# Introduction

The study of the nuclear structure of doubly-magic nuclei and relevant neighboring isotopes is an effective method to set light on the role of the nucleon-nucleon interaction in the collective behavior of the nucleus. Of high interest in this context is the robustness of the proton Z = 50 shell closure when the N = 50 magic numbers are approached. While the experimental access to the self-conjugate doubly-magic $^{100}$Sn is still limited, most of the data obtained stems from the nuclei in the neighborhood.

Shell-model calculations with the CD-Bonn [1] interaction in the full N=50-N=82 valence space show that the quadrupole strength of core-coupled states in odd-even nuclei closely follow the general trend of the corresponding even-even isotopes for the $2^+$ states. Considering that a recent direct measurement of the lifetime of the $2_1{}^+$ and the $4_1{}^+$ excited states in $^{106,108}$Sn was performed via a multi-nucleon transfer reaction for the very first time [2], the odd-even $^{105}$Sn isotope provides a unique opportunity for direct lifetime measurements of low-lying levels in odd Sn isotopes close to $^{100}$Sn [3].

In order to extend our information on the $^{100}$Sn region, in particular the $^{105}$Sn isotope, an experiment was performed at the Laboratori Nazionali di Legnaro (LNL) to investigate the lifetimes of excited states of the exotic neutron-deficient

Sn, In, Cd isotopes. In this research, the neutron-deficient Sn region was populated via a fusion-evaporation reaction with a 180 MeV beam of $^{50}$Cr impinging on a $^{58}$Ni target. The $\gamma$ rays emitted by the high-spin states of the populated nuclei were detected with the $\gamma$-ray array GALILEO coupled to the light-charged-particle detector array EUCLIDES and the dedicated GALILEO plunger device, emploiting the coincidence Recoil Distance Doppler Shift (RDDS) technique. The experiment will be discussed in detail in Chapter 3.

Thanks to the large statistics in this experiment and well known low-lying states along the isotopic In and Cd chain, the lifetimes of the low-lying excited states of $^{105}$In and $^{104}$Cd populated through the reaction channels $^{50}$Cr($^{58}$Ni, $3p$)$^{105}$In and $^{50}$Cr($^{58}$Ni, $4p$)$^{104}$Cd are extracted and compared to previously known values to demonstrate the feasibility of the adopted experimental technique [3]. In order to reduce the error of the extracted results, for the $17/2^+$ state of $^{105}$In a test on both Decay-Curve Method (DCM) and Differential Decay-Curve Method (DDCM) will be discussed. The applicability of these two methods will be clarified in chapter 4.

The relevant part of the level schemes of $^{105}$In and $^{104}$Cd are presented in Fig. 1.1 and Fig. 1.2, respectively. To facilitate the contaminants recognizition in the lifetime analysis in Chapter 5, the partial level scheme of $^{102}$Cd for the ground state band is also presented in Fig. 1.3. Earlier published work has confirmed and established lifetimes and lifetime limits of yrast states in $^{105}$In [4] and $^{104}$Cd [5] with small errors. Parallel to the experimental progress, the understanding of excited states of nearly spherical nuclei in the $^{100}$Sn region has been improved by shell model calculations, adopted values in the nuclear data sheets for A=102, 104 and 105 isotopes [6, 7, 8] are used as references in the present work.

In addition, as an expansion in the scope of the project, the dipole structure of the N = 56 isotone $^{104}$Cd have been investigated. In the nearly spherical nuclei $^{104}$Cd, a high-lying band characterized by strong magnetic dipole ($M1$) transitions with weak or absent $E2$ crossover transitions have been observed from our experimental spectroscopic data, which is indicated as band 1 in Fig. 5.10. The very weak $E2$

crossover transitions point to a small deformation. These experimental properties fulfill the basic conditions of a magnetic rotational structure [10]. Therefore, the manifestation of the magnetic rotation (MR) might be expected in $^{104}$Cd, which is an exotic rotational phenomenon observed in weakly deformed or near-spherical nuclei and differs from conventional collective rotation in well-deformed nuclei. The information of $B(M1)$ strengths of the states in the $M1$ bands will help to shed more light on their structure. Lifetimes of two high-spin states in $^{104}$Cd have been measured with the aim to investigate the possible incipient magnetic rotation.

The relative richness in available data on excited-state energies is in contrast to the limited corresponding knowledge of transition probabilities. Such information, although more difficult to obtain experimentally, is crucial for testing theoretical models and understanding the structure of the nucleus in a decisive way.

The present work was contextualized in understanding, in a systematic way, the changes in structural phenomena as one moves from the semi-magic Sn isotopes to transitional nuclei at Z = 49 and 48 in the $^{100}$Sn region.

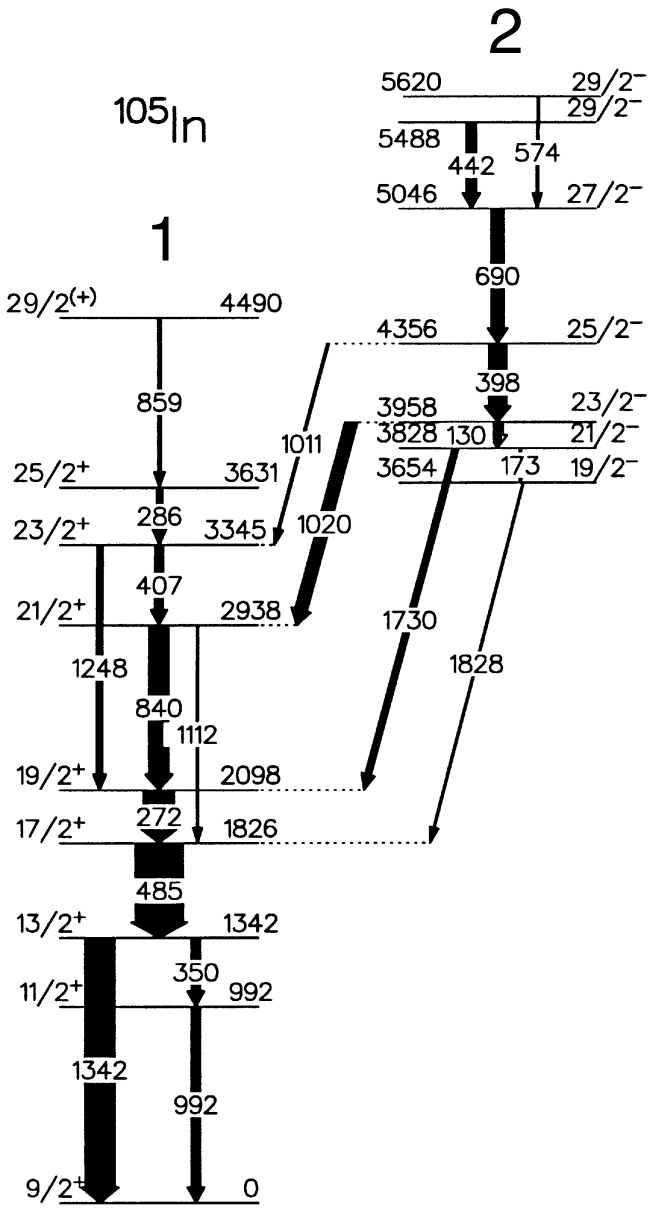


**Figure 1.1:** Partial level schemes showing the ground state band and first negative parity band for $^{105}$In. The width of the arrows is proportional to the measured or calculated transition probability. Figure adopted from Reference [4]. The excited state at 4490 keV is assigned a spin/parity of $29/2^+$ here instead of $27/2^+$ as suggested in Ref. [9].

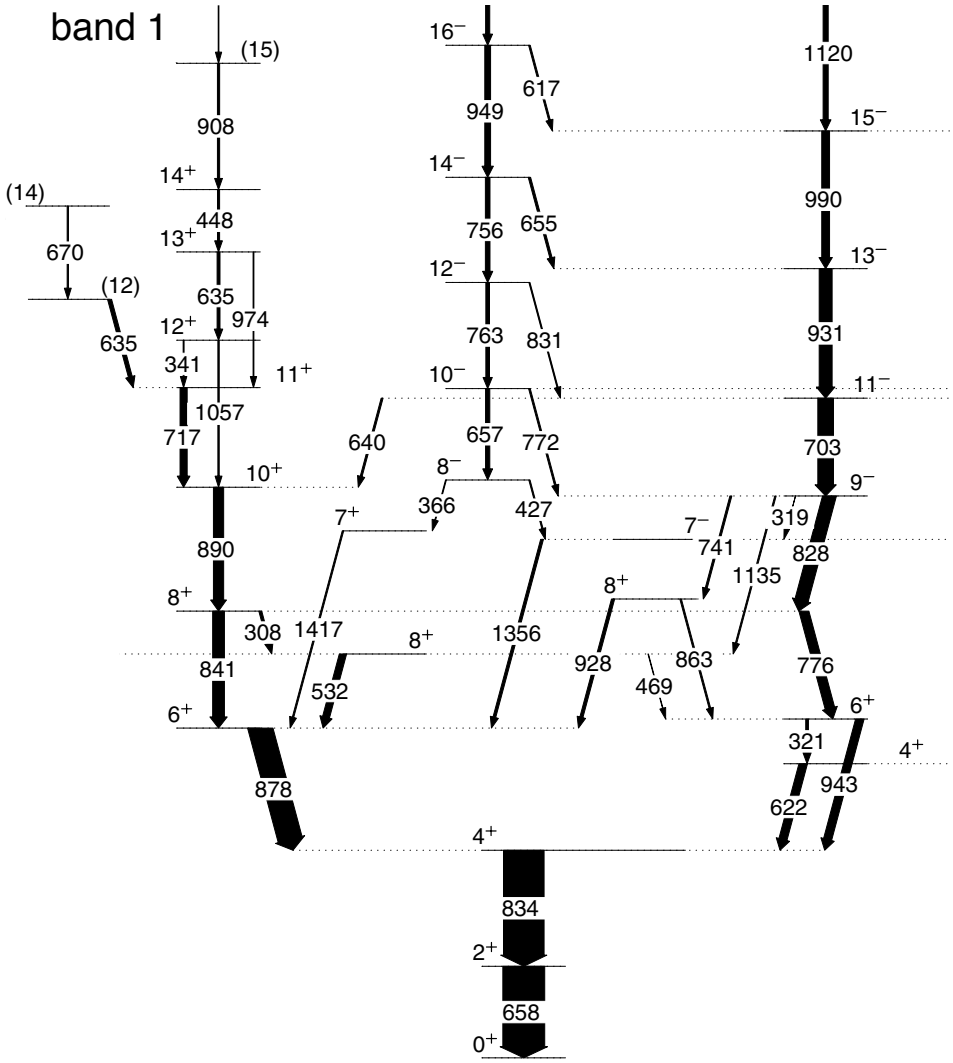


**Figure 1.2:** Partial level schemes showing the low-lying states and band 1 based on $6^+$ state for $^{104}$Cd. The width of the arrows is proportional to the measured or calculated transition probability. Figure taken from Nuclear Data Sheets [7].

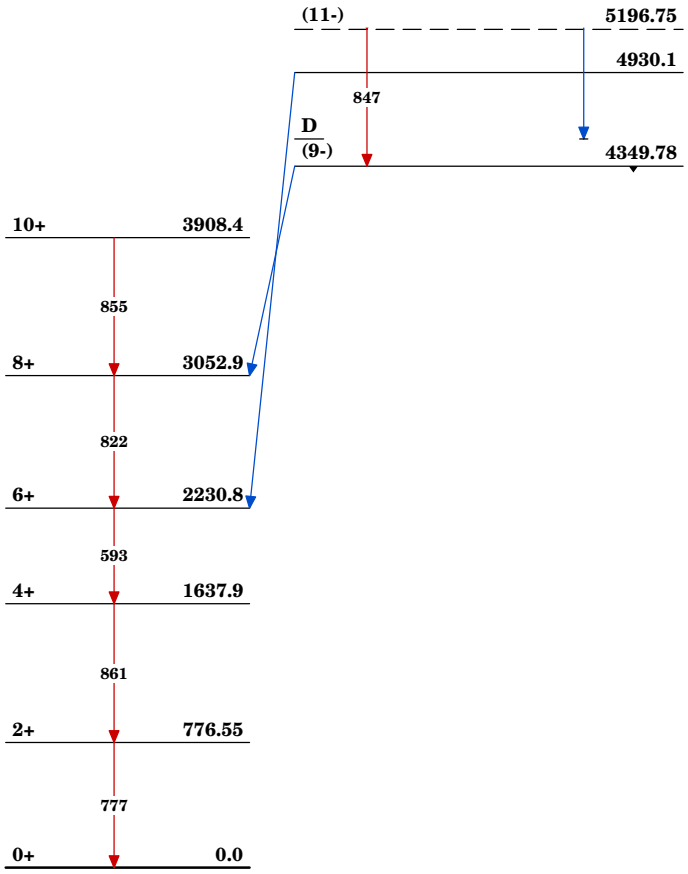


**Figure 1.3:** Partial level scheme showing the ground state band of $^{102}$Cd. Figure taken from [6].

# Chapter 2

# Background and Theoretical Framework

In the last decades, the experimental investigation of excited states of nuclei in the vicinity of the Z = N = 50 double-shell closure have resulted in a remarkable gain in our understanding of the structure of the nucleus. Through the investigation of the coupling of the a few of valence nucleons or holes to the doubly magic $^{100}$Sn core, information on the shell model parameters can be derived from the experimental observables, such as single-particle energies, reduced transition probabilities and quadrupole moments [11], and it can be used to predict the structure of more complex nuclear configurations. Thus, experimental data are needed in order to make robust predictions.

Being in the close vicinity of the doubly-magic Z = N = 50 core $^{100}$Sn, the low spin states in light In and Cd isotopes are generated predominantly by single-particle excitations. The angular momentum of the states increase along the band is generated by the simultaneous reorientation of the spins of the proton holes and of the neutron particles, as the shell model predicts in the $n($ $p_{1/2}$, $g_{9/2}$ $)$ $v(d_{5/2}$, $g_{7/2}$, $s_{1/2}$, $d_{3/2}$, $h_{11/2})$ configuration space [12]. The low spin states in $^{105}$In and $^{104}$Cd have been explained successfully in the framework of the nuclear shell model [9, 5]. The well known lifetimes of their low-lying states are used as benchmark of

the experimental technique.

However, the $B(M1)$ strengths measured for a few states in the $\Delta I = 1$ band of $^{105}$In, marked as "band 1" in Fig. 1.1, fail to agree with shell-model calculations [9]. These observations indicate that there are other possible excitation mechanisms responsible for the generation of spin in this sequence. One possible mode of excitation is the “shears mechanism" (or magnetic rotation). A typical property of the magnetic rotation (MR) bands is the decreasing and finally vanish of the $B(M1)$ values with increasing spin. Such behaviour of the $B(M1)$ strengths, which are a sensitive probe of the magnetic rotation band, can be inferred from lifetime measurements. In general, it has been found that the shears mechanism is active in heavier isotopes while it becomes less prominent until almost vanish for lower-mass isotopes in the near spherical nuclei in the A $\sim$ 110 mass region. Since the manifestation of the MR bands have been confirmed in $^{108}$Cd and $^{107}$In from the previous review [13] and recent observation [14], the nuclei $^{104}$Cd and $^{105}$In might be good testing grounds for the investigation of the lower boundary for the appearance of magnetic rotation in Cd and In isotopic chains, respectively.

The physical motivations for the present study and its relevance in the field of modern nuclear physics are introduced in the next sections.

## 2.1 The nuclear model

### 2.1.1 Nuclear Hamiltonian

In the nucleus the protons and neutrons interact with each other and form a many body system. The non-relativistic Hamiltonian for A nucleons can be written as [15]:

$$H = \sum_{i=1}^{A} T_i + \sum_{i,j}^{A} V_{ij} \tag{2.1}$$

where $T_i$ denotes the kinetic energy of every single nucleon and $V_{ij}$ is the two-body interaction potential. The eigenvalues and corresponding eigenvectors give rise to

an energy spectrum in which each energy level can be characterised by excitation energy, total spin $I$ and parity $\pi$: $I^{\pi}$ [15].

By assuming the existence of a single-particle potential $V_{ij}$, the Hamiltonian can be separated into a single-particle Hamiltonian with remaining residual interactions. A numerical solution therefore becomes possible.

$$H = (\sum_{i=1}^{A} T_i + \sum_{i,j}^{A} V_i) + (\sum_{i,j}^{A} V_{ij} - \sum_{i,j}^{A} V_i) = \sum_{i=1}^{A} H_i^{s.p.} + \sum_{i,j}^{A} H_{ij}^{res} \tag{2.2}$$

### 2.1.2 Nuclear shell model

Similiar to the effects of electron shells observed in atoms, nuclei exhibit enhanced stability and a sharp increase in binding energy at certain values of proton and neutron numbers which are called "magic numbers". In the nuclear shell model, each nucleon is assumed to be moving in an external field, created by the remaining A  1 nucleons and the mean-field potential is represented by a 3D harmonic oscillator potential along with the spin-orbit interaction [15]. As a consequence, the magic numbers (Z or N = 2, 8, 20, 28, 50, 82 and 126) are correctly reproduced. In the shell model calculations, nuclei are always modeled as an inert core at the magic numbers of tightly bound nucleons and a valence space with more readily excitable nucleons. The nuclear shell structure indicating the shell closure is shown in Fig. 2.1.

**The Z=50 Shell Closure**

As per the shell model description after spin orbit coupling $^{100}$Sn is a double shell-closure nuclei with N = Z = 50.

The structure of $^{105}$In and $^{104}$Cd can be described within the shell model considering one and two proton holes in the Z=50 core and 6 valence neutrons outside the N = 50 core, respectively. We consider the two proton orbitals between Z = 38 and 50, $p_{1/2}$, $g_{9/2}$, and the five neutron orbitals between N = 50 and 82, $d_{5/2}$, $g_{7/2}$, $s_{1/2}$,

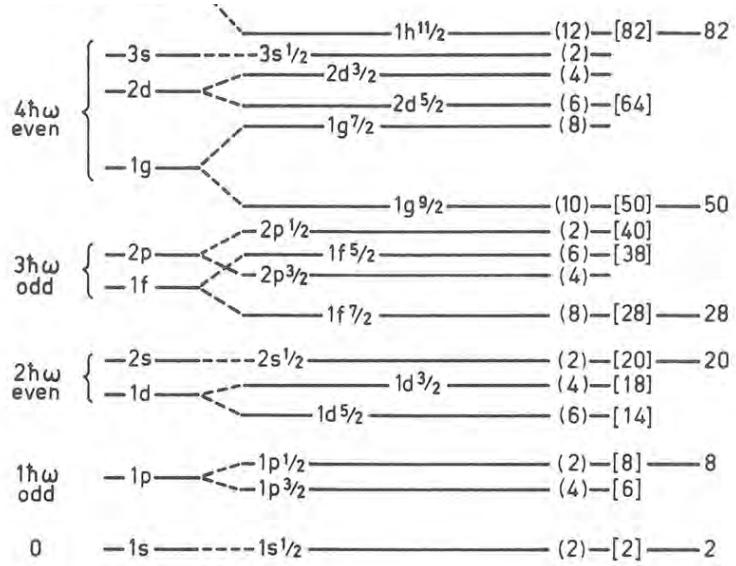


**Figure 2.1:** Single-particle levels when the spin-orbit term is added to the harmonic oscillator Hamiltonian. The shell effect is quite apparent, and the magic numbers are exactly reproduced.

$d_{3/2}$, $h_{11/2}$, as the valence orbits. The $s_{1/2}$ and $d_{3/2}$ orbits are not very crucial for high spin states and the $h_{11/2}$ intruder orbit is expected to contribute to the main components of the negative parity states [16].

Theoretical calculations within the nuclear shell model have been performed in previous work for the neutron deficient Cd muclei from N = 50 through N = 58 and $^{104,105}$In [17, 9]. For the low-lying states, the shell model were proved to be able to reconstruct the energy spectrum very well and calculate reduced transition probabilities that are comparable to the experimental values.

## 2.2 Magnetic dipole bands in near spherical nuclei

The magnetic rotation [10], which are observed as exotic rotational phenomenon in some weakly deformed or near-spherical nuclei, has been of great interest since the observation of “shears” bands in the region of neutron-deficient Pb isotopes in

the 1990s [10]. Experimentally, more than 200 magnetic rotational bands spread over the A $\sim$ 80, 110, 130, and 190 mass regions have been identified so far.

The Tilted Axis Cranking (TAC) model [10] provides the theoretical framework for a description of magnetic rotation. Different from normal rotation, here the magnetic dipole arises from proton particles (holes) and neutron holes (particles) in high-$j$ orbitals which rotate around the total angular-momentum vector and not the deformed electrical charge distribution. For the nuclei with Z <50, N > 50 in the A $\sim$ 110 region, neutron-particles in the $h_{11/2}$ orbital and proton-holes in the $g_{9/2}$ orbital combine to the rotating dipole. The results of the TAC calculation indicates that the basic configuration of the $\Delta I = 1$ bands consist of a proton hole in the $g_{9/2}$ orbital coupled with one neutron in the $h_{11/2}$ orbital in case of negative parity bands, or two $vh_{11/2}$ for the positive parity ones [18].

The physics of the magnetic rotational bands is sketched in Fig. 2.2. At the bandhead, the proton angular momentum vector $j^{\pi}$ is nearly perpendicular to the neutron angular momentum vector $j^{v}$. Higher angular momentum states result as $j^{\pi}$ and $j^{v}$ align toward the total angular momentum vector $I$ with increasing spin, which reduces the perpendicular component of the magnetic dipole moment, $\mu_{\perp}$. This resembles the closing of the blades of a pair of shears, hence the name "shears mechanism" for the excitation mode. Consequently, the $B(M1)$ values, which is proportional to $\mu_{\perp}^{2}$, should exhibit a characteristic decline with increasing angular momentum. This behavior of the $B(M1)$ values is the crucial experimental signature of the shears mechanism. Instead, if the $M1$ bands arise from the collective rotation of a weakly oblate shape, then the $B(M1)$ values are expected to be rather constant.

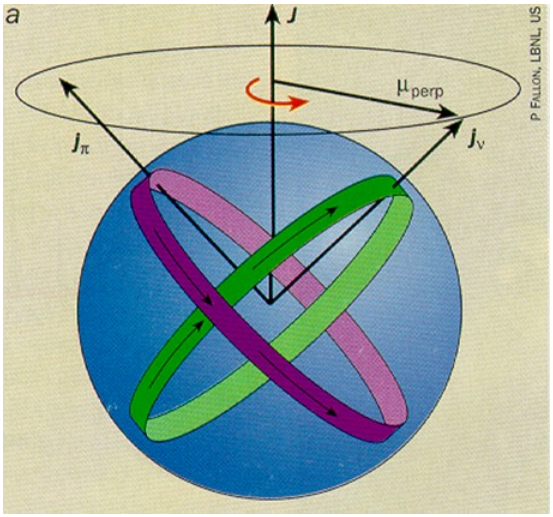


**Figure 2.2:** Schematic of the angular momentum coupling between high-$j$ protons and neutrons orbitals in a shears band.

## 2.3 Nuclear structure from gamma-ray spectroscopy

The various electromagnetic observables probe the structure of the wave functions involved through multipole moments and gamma decays [19]. The decay properties of electromagnetic observables are good indicators of the degree of validity of various assumptions underlying the structure of nuclear states.

### 2.3.1 Nuclear excited states and electromagnetic transitions

The energy of an electromagnetic radiation field can be described mathematically in terms of a multipole moment expansion. In general, electric (charge) radiation or magnetic (current, magnetic moment) radiation can be classified into multipoles E$\lambda$ (electric) or M$\lambda$ (magnetic) of order $2^{\lambda}$ , e.g., $\lambda = 1$ for dipole, $\lambda = 2$ for quadrupole, or $\lambda = 3$ for octupole, etc, where $\lambda$ is the multipolarity of the energy allowed electromagnetic radiation, limited to $|I_i - I_f| < \lambda < I_i + I_f$, $I_i$ and $I_f$ are the spin of the initial and final states, respectively. The expansion converges rapidly, hence only the lower orders are of importance.

The multipole moments are dependent on charge and current densities in the nucleus and so their study allows information to be extracted on these properties. When we compute the expectation value of a appropriate electromagnetic operator, all odd-parity static multipole moments must vanish – odd-order electric moments with parity $(-1)^{\lambda}$ and even-order magnetic moments with parity $(-1)^{\lambda+1}$. Therefore two multipole moments are of great consideration for studying the excitation mechanisms in the nuclei: the magnetic dipole ($M1$) moments which are sensitive to nuclear magnetic moments and single-particle properties, and the electric quadrupole ($E2$) moments sensitive to both the single-particle properties and collective effects such as deformation.

It is therefore critical to investigate the reduced electromagnetic transition strengths $B(M1)$ and $B(E2)$ both from experimental and theoretical perspectives.

### 2.3.2 Transition probability and mean lifetime

Consider an electromagnetic gamma transition from an initial nuclear state $i$ to a final nuclear state $f$, the transition probability $T_{fi}$, decays per second, allows one to extract the electromagnetic transition rate.

The mean lifetime $\tau$ (or half-life $t_{1/2} = (\ln 2)\tau$) of a decaying level, which can be measured in a direct timing method like the RDDS method, is simply

$$\tau = T^{-1} \tag{2.3}$$

For a specific energy allowed electromagnetic radiation, the transition rate can be easily related to the reduced transition probability $B(^{M}_{E}\lambda)$ [19]

$$T_{fi}^{(^{M}_{E}\lambda)} = \frac{8\pi}{\hbar}\frac{\lambda+1}{\lambda[(2\lambda+1)!!]^2}\left(\frac{E_\gamma}{\hbar c}\right)^{2\lambda+1} B(^{M}_{E}\lambda; I_i \rightarrow I_f) \tag{2.4}$$

Thus consider an excited level $i$ deexcited to state $f$, the reduced transition probability is proportional to the reciprocal of the mean lifetime of the initial state. By determining the mean lifetime $\tau$ from a lifetime measurement, the "experimental" value for the reduced transition probability of the of the $\gamma$-ray with multipolarity $\lambda$ and energy $E_\gamma$ can be deduced.

### 2.3.3 Adopted values of reduced transition probabilities

Consider a transition between nuclear states with the theoretical predictions of nuclear models, the reduced transition probability is proportional to the square of the reduced transition matrix element between the states [20]:

$$B(^{M}_{E}\lambda; I_i \rightarrow I_f) = \frac{1}{2I_i+1}|\left\langle I_f||M(^{M}_{E}\lambda)||I_i\right\rangle|^2 \tag{2.5}$$

where $M(^{M}_{E}\lambda)$ is the electric or magnetic multipole operator and $^{M}_{E}\lambda$ refers to the mode of transition and its multipolarity, $\lambda$. Compared to the matrix element, the

reduced matrix element $\left\langle I_f||M(^M_E\lambda)||I_i\right\rangle$ removes the dependence on the magnetic quantum numbers and therefore contains only the intrinsic nuclear information.

By means of the well know electromagnetic operator $M(^M_E\lambda)$, a theoretical, i.e. a calculated value $B(^M_E\lambda)_{THOER}$ can be provided for the respective reduced transition probability by the model in consideration. Hence, according to equations 2.4 and 2.5, by comparing experimental $B(^M_E\lambda)$ values with theoretically calculated ones, different nuclear models can be tested, as shown in Fig. 2.3.

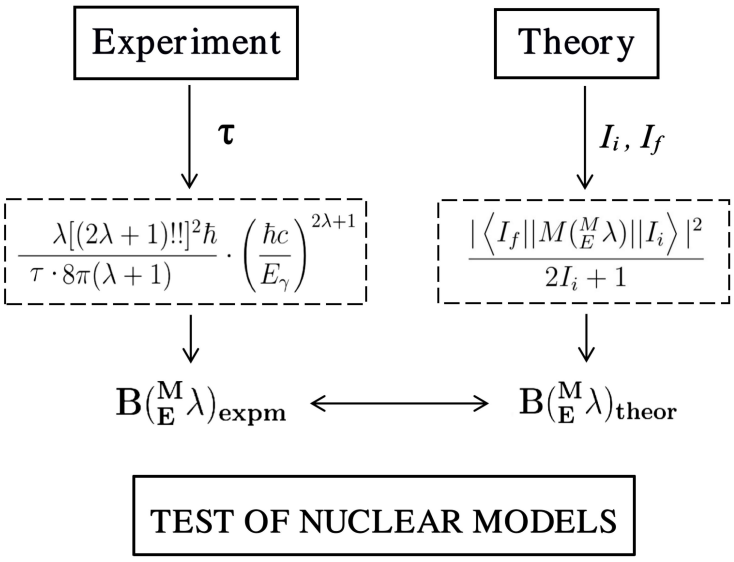


**Figure 2.3:** The goal of lifetime measurements.

The transition rate $T(^{M}_{E}\lambda)$, decays per second, for a specific multipole can be easily related to the reduced transition probabilities [20]. $T(^{M}_{E}\lambda)$ for the lower orders of multipoles which are of importance are shown in Table 2.1 and Table 2.2.

**Single-Particle Transitions**

An electric single-particle transition: assume excitation of only one proton in an average central potential that changes orbit from $j_i$ to $j_f$. A magnetic single-particle transition takes place when the intrinsic spin is flipped, e.g. $j_i = I_i + 1/2$ and $j_f = I_f$ -1/2. Using the Weisskopf estimates for reduced transition probabilities, the following characters of the single-particle transition rates are found:

- Low multipolarities are favoured.
- Electric transitions are faster than magnetic transitions.

For convenience, the set of formulas relating the transition probabilities $T$ in $s^{-1}$, $\tau$ in s, the reduced transition probabilities $B(E\lambda)$ in $e^2fm^{2\lambda}$, $B(M\lambda)$ in $(\mu_N/c)^2fm^{2\lambda-2}$ for the transition with $E_\gamma$ in MeV are given in Table 2.1 and Table 2.2 for the first few values of $\lambda$.

| $E\lambda$ | $T(E\lambda) = \frac{1}{\tau_{E\lambda}}$ | $B_W(E\lambda)$ |
|---|---|---|
| E1 | $1.587 \times 10^{15} {E_\gamma}^3 B(E1)$ | $0.06446A^{2/3}$ |
| E2 | $1.223 \times 10^{9} {E_\gamma}^5 B(E2)$ | $0.05940A^{4/3}$ |
| E3 | $5.698 \times 10^{2} {E_\gamma}^7 B(E3)$ | $0.05940A^{2}$ |

**Table 2.1:** Transition probabilities and the Weisskopf estimates for the lowest $E\lambda$ transitions.

In the lifetime measurement, once the state of interest was populated, it will remain excited for a mean lifetime $\tau$ which can be simply related to the decay probability [21]:

$$\tau(^{M}_{E}\lambda) = T(^{M}_{E}\lambda)^{-1} \tag{2.6}$$

| $M\lambda$ | $T(M\lambda) = \frac{1}{\tau_{M\lambda}}$ | $B_W(M\lambda)$ |
|---|---|---|
| $M1$ | $1.779 \times 10^{13} {E_\gamma}^3 B(M1)$ | 1.790 |
| $M2$ | $1.371 \times 10^{7} {E_\gamma}^5 B(M2)$ | $1.650A^{2/3}$ |
| $M3$ | $6.387 \times 10^{0} {E_\gamma}^7 B(M3)$ | $1.650A^{4/3}$ |

**Table 2.2:** Transition probabilities and the Weisskopf estimates for the lowest $M\lambda$ transitions.

The partial lifetime $\tau_\gamma$ of a particular transition can be calculated with the knowledge of the branchig-ratio by the relation

$$\tau(^{M}_{E}\lambda) = \tau_{exp} \frac{I_{total}}{I_\gamma(^{M}_{E}\lambda)} \tag{2.7}$$

where $\tau_{exp}$ is the experimentally measured lifetime of the level of interest, $I_\gamma(^{M}_{E}\lambda)$ is the intensity of the transition of interest and $I_{tot}$ is the intensities of all the gamma transitions depopulating the level.

This thesis will focus on the measurement of the reduced transition probabilites of the $E2$ and $M1$ transitions which can be obtain via lifetime measurements, for the reason that the two strengths give particularly valuable insights into the nature of nuclear collectivity and its evolution with respect to the neutron (N) and proton (Z) numbers.

## 2.4 Lifetime measurement

The importance of lifetime measurements of nuclear levels has been recognized for a long time. The techniques employed to measure lifetimes, or absolute transition probabilities, are very simple conceptually but are ingeniously adapted to obtain sensitivity to the decay products and to cover an enormous time scale from $10^{-20}$ s to many years [22]. In particular, the well established and widely applied RDDS method which is possible to obtain lifetimes in the range $10^{-9} - 10^{-12}$ s is performed in this experiment.

Figure 2.4 shows the general range of lifetimes that can be measured using the various established methods. These methods have been divided into two groups: those that measure transition probabilities directly, and those that measure lifetimes. Typically, general estimates for the expected lifetimes can be inferred using trends in nearby nuclei, however this is not the only factor one must consider when deciding a method. The main limitation often depends on how one intends to populate excited states in the isotope of interest. In this project, the proposed experiment was employed a fusion-evaporation reaction (see Section 4.1) and the isotope of interest was predicted to have lifetimes in the order of ps. Thus, the Recoil Distance Doppler Shift (RDDS) method presented the most advantages and will be a key topic in the upcoming discussion. The RDDS method employs a dedicated plunger device for the lifetime measurement, the analysis will be discussed in detail in Chapter 5.

In the RDDS method the lifetime of the excited level emitting a $\gamma$-ray is compared with the time taken for the recoil to travel in vacuo between two foils separated by distances in the range of 5 $\mu$m to 2 cm.

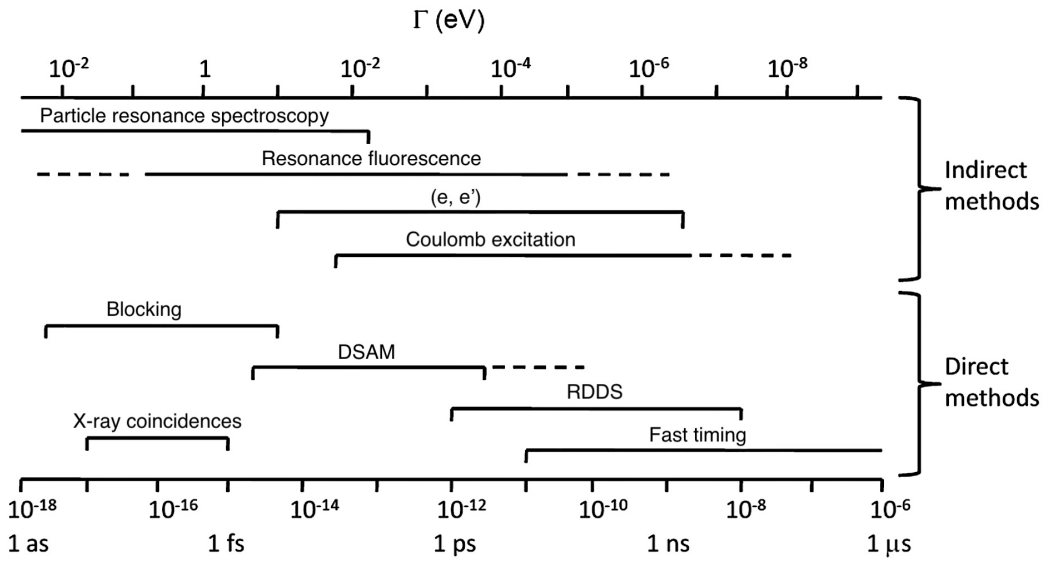


**Figure 2.4:** Figure showing the general regions over which different methods of lifetime measurement are best employed. The methods have been split into those that directly measure transition matrix elements. [23]

# Chapter 3

# Experimental Setup

In this chapter the nuclear reaction populating the region of interest and the experimental setup will be presented. The experiment was performed at Laboratori Nazionali di Legnaro (LNL). The neutron deficient isotopes of interest were populated via a fusion evaporation reaction using a 180 MeV $^{50}$Cr beam and a $^{58}$Ni target of 1 mg/cm$^2$ thickness.

A highly selective setup composed of the $\gamma$-ray array GALILEO [24] coupled with the charged particles detector array EUCLIDES [24, 25] and a dedicated plunger device [26] for GALILEO was employed, it was optimized to yield high selectivity for different reaction channels and study the very neutron-deficient nuclei free from background. A schematic view of the experimental apparatus is shown in fig. 3.1.

## 3.1 Fusion-evaporation reactions

The classical method to investigate neutron-deficient nuclei at the N $\sim$ Z region is the in-beam spectroscopy following fusion-evaporation reactions. It is characterized by large angular momentum transfer to the compound nucleus and the evaporation residues emitted into a narrow cone at forward angles.

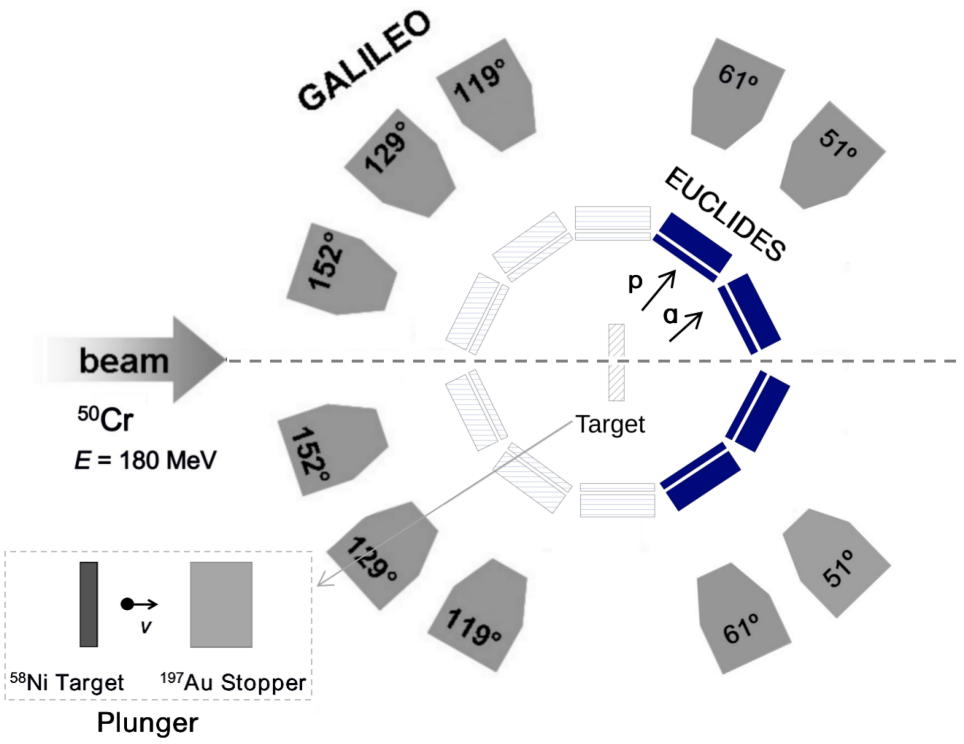


**Figure 3.1:** Schematic view of GALILEO $\gamma$-ray spectrometer coupled to EUCLIDES. The target is installed at the centre of the vacuum reaction chamber. The hatched part of ECULIDES is dismounted to allow plunger installation.

The nuclei of interest are typically produced in complete fusion reaction of heavy-ions at the Coulomb barrier. After the complete fusion, the decay of unstable compound nuclei will quickly evaporate protons, neutrons or alpha particles repeatedly until reaching more stable nuclei. A fusion evaporation reaction usually populates compound nucleus at high energy and high spin, as a consequence, the light particle evaporation path to reach the low lying isotopes is often complex. Therefore each fusion-evaporation reaction can go multiple different ways, resulting in different isotopes being produced, known as output channels. A schematic diagram, presented in Fig. 3.2, shows the production and decay mechanism of a compound nucleus.

Typical reactions and compound nuclei on the way towards $^{100}$Sn are $^{46}$Ti + $^{58}$Ni $\rightarrow^{104}$Sn*, $^{50}$Cr + $^{58}$Ni $\rightarrow^{108}$Te*, $^{64}$Zn + $^{36}$Ar $\rightarrow^{100}$Cd* and $^{40}$Ca + $^{58}$Ni $\rightarrow^{98}$Cd* at bombarding energies of 3.5 – 4.5 MeV/A, above the Coulomb barrier.

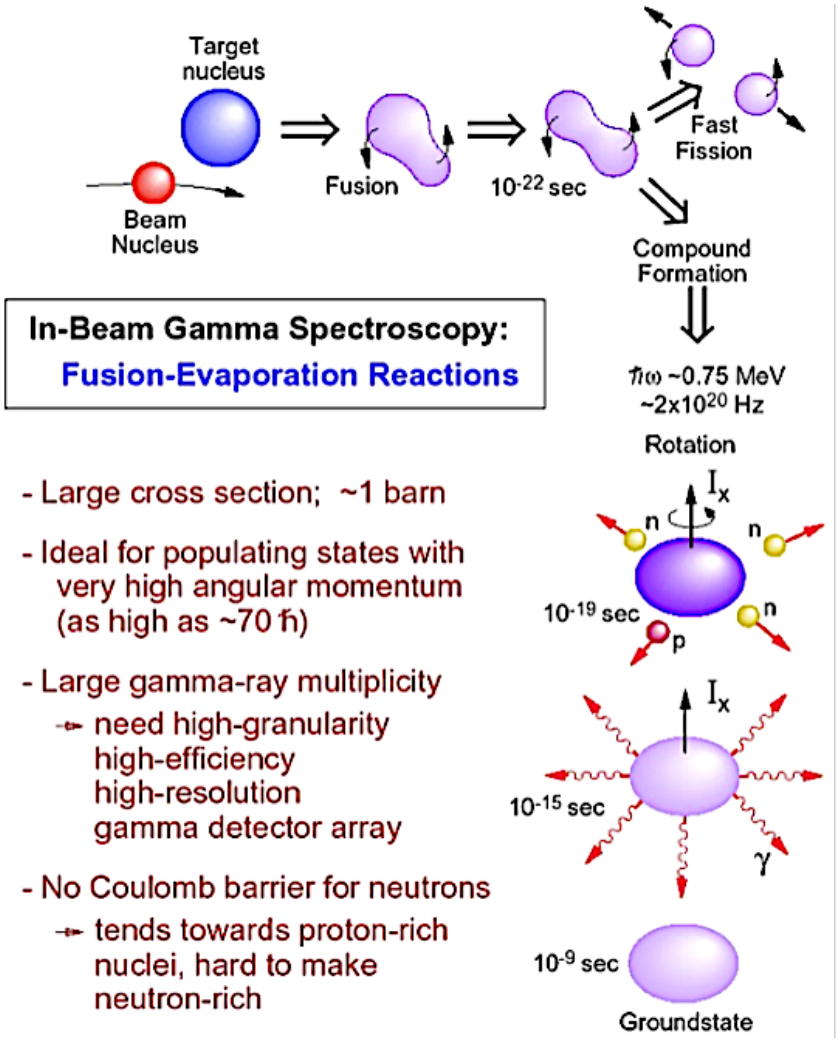


**Figure 3.2:** The production and decay mechanism of a compound nucleus in Fusion-evaporation reaction, with the average time scale of each step indicated. Figure adapted from Reference [27].

In the discussed experiment, the excited states of $^{105}$Sn were populated via the fusion-evaporation reaction $^{50}$Cr($^{58}$Ni, $2p1n$)$^{105}$Sn. The primary 180 MeV $^{50}$Cr beam was provided by the Tandem XTU accelerator of the Legnaro National Laboratory and delivered to a 1 mg/cm$^2$ thickness $^{58}$Ni target inside the GALILEO spectrometer. Besides the $^{105}$Sn, this reactions opened different channels with different number of protons and/or neutrons emitted from the $^{108}$Te compound nucleus: $^{105}$In($3p$), $^{104}$Cd($4p$), $^{102}$Cd($1\alpha 2p$). These various reaction products identified from our experiment data are shown in Fig. 3.3. The details of the

contaminants identification and channel selection will be presented in Chapter 4.

Since the most exotic exit channels are produced by evaporation of mostly neutrons (apart from protons and alpha-particles) from the compound nucleus with very low cross sections in the sub-millibarn to microbarn region as compared with about one barn of the total reaction cross section, a highly selective setup is needed. In the presented experiment, the GALILEO-EUCLIDES-Plunger setup was optimized to yield high selectivity for different reaction channels and study the very neutron-deficient nuclei free from background.

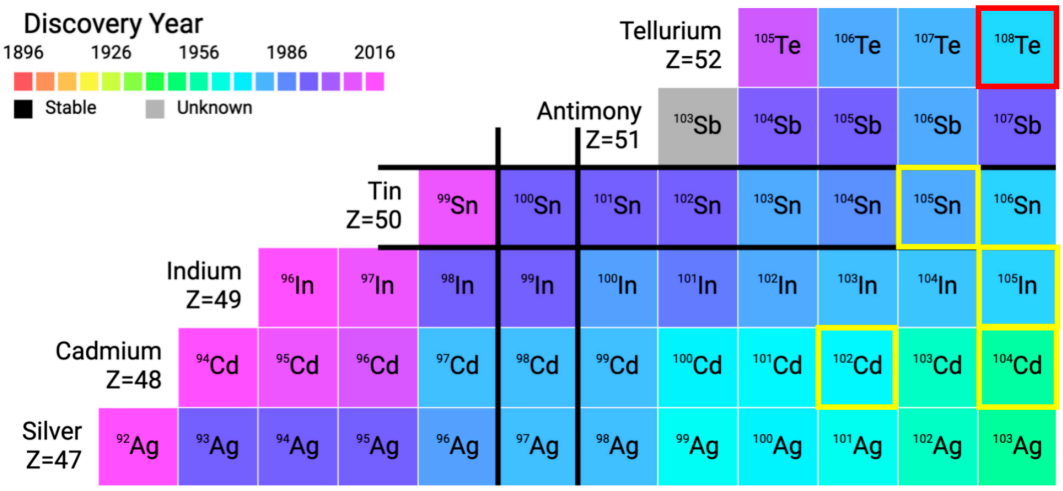


**Figure 3.3:** Region of the nuclear chart accessible via the reaction employed in the experiment, colour coded by discovery year. The compound nucleus $^{108}$Te is highlighted in red, while the various reaction products are highlighted in yellow. The Figure was produced using [28].

## 3.2 GALILEO spectrometer

The GALILEO $\gamma$-ray spectrometer [24] has been constructed as a $4\pi$ high-resolution $\gamma$- ray array at the Legnaro National Laboratory of INFN (LNL-INFN) and used to investigate nuclear structure via in-beam $\gamma$-ray spectroscopy methods [24]. The GALILEO development has been divided in two phases. GALILEO

phase I has a symmetric geometry of 25 Compton-suppressed high-purity germanium (HPGe) tapered detectors with respect to the beam axis. In the second phase, 5 additional HPGe tapered detectors (for a total of 30) and 10 triple cluster detectors will be added to complete the spectrometer [24]

. At the time of this experiment, the 25 GALILEO detectors were organized into 5 rings: three backward rings at $\theta_0$=152°, $\theta_1$=129°and $\theta_2$=119°, two forward rings at $\theta_4$=61°and $\theta_5$=51° to the beam line, respectively, each ring consists of 5 detectors. Therefore excited-state lifetimes for each ring can be estimated, as the energy shift of the $\gamma$-ray emitted in-flight depends on the direction of emission. In the analysis, a weighted average of the lifetimes for different rings can be extracted, leading to a more precise measurement.

**Figure 3.4:** Photo of one HPGe detectors ring of GALILEO $\gamma$-ray spectrometer inside BGO shield placed around the reaction chamber. The EUCLIDES Si-ball and the plunger is inserted in the reaction chamber of GALILEO. Figure adapted from Reference [24].

Four $LaBr_3$ scintillators for fast timing were also placed at 90° with respect to the beam direction to obtain a complementary estimation of the excited state with lifetimes in the orders from nanoseconds to tens of picoseconds, which is the case of first excited state $7/2^+$ of $^{105}$Sn. A precise remeasurement of this lifetime will possibly shed light on the controversy regarding the spin-parity assignments of the ground state $5/2^+$ and/or first excited state $7/2^+$, for odd Sn isotopes in the $^{100}$Sn region [3].

HPGe detectors are characterized by an excellent energy resolution and therefore are able to produce spectra with well-defined narrow peaks. For this reason they are largely used in gamma-ray spectroscopy where the energies of the typical in-beam $\gamma$-rays are between a few tens of keV to a few MeV [29]. In particular, for the 1332 keV $\gamma$ ray emitted by the stationary $^{60}$Co source, a full energy peak (FEP) detection efficiency of ∼2.4% and an average energy resolution of ∼2.4 keV (FWHM) were measured for the full GALILEO array in previous experiment. [30]. The energy resolution will be one reference for the energy width of the gates to construct the $\gamma$-$\gamma$ coincidence spectra in the data analysis (see Chapter 4.2). However, the HPGe detectors must be cooled with liquid nitrogen to avoid the current leakage across the band-gap due to thermal agitation.

With the purpose to increase the peak–to–total ratio for the whole GALILEO array, the high-purity germanium (HPGe) detectors are surrounded by bismuth germanate (BGO) crystals which act as anti-Compton shields. Since in the case of scintillation material, high Z and high density entail the large probability per unit volume for the photoelectric absorption of $\gamma$ ray [29], BGO was chosen for its very high detection efficiency. Each HPGe detectors of GALILEO is surrounded by eight BGOs [31], as shown in Fig. 3.5. When an event is detected by a BGO anti-Compton shield in coincidence with the HPGe detector inside, it means that the photon did not deposit all of its energy in the HPGe. Therefore, unwanted events which do not correspond to to full photopeak absorption can be rejected to avoid the incorrect estimation of the energy. Consequently, for the whole

GALILEO array, a peak–to–total ratio of about 50% has been achieved [26]. However, this comes at the cost of reduced geometric efficiency of the array since the usage of the anti-Compton shields sacrifices the solid angle coverage.

These 25 HPGe/BGO detector modules were mounted at 22.5 cm from the target position [24]. At the center of GALILEO is the vacuum reaction chamber, which contains enough space to place the target and ancillary detectors such as EUCLIDES and the dedicated plunger device in this experiment. According to the different reaction products of different experiments, the versatile design of the GALILEO array enables the coupling with one or more ancillary devices in order to improve the selectivity, making it possible to detect rare exotic process at much higher resolving power than simple $\gamma$-detection.

The GALILEO Data Acquisition (DAQ) system is fully digital and it is synchronized by a distributed clock delivered by the GTS (Global Trigger and Synchronization) system, which enables the time synchronization between the GALILEO spectrometer and all other ancillary detectors [24]. The data acquisition (DAQ) software used for GALILEO is based on the XDAQ framework [32].

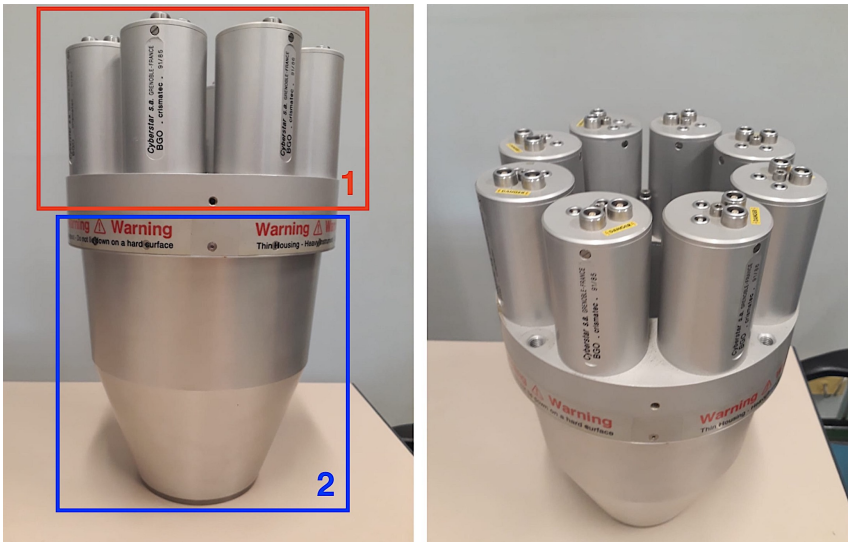


**Figure 3.5:** Photo of a BGO anti-Compton shield of GALILEO. Left: 1. Photomultiplier Tubes; 2. Bismuth Germanate Crystals. Right: view of the eight BGOs. Figure taken from Reference [30].

## 3.3 EUCLIDES

The light-charged-particle detector array EUCLIDES [25] based on the ΔE-E telescopes allows the detection and discrimination between light charged particles thanks to the ΔE-E technique. The moderate-dimension EUCLIDES Si-ball array can be installed inside the vacuum reaction chamber of GALILEO in the full or in the plunger configuration [26]. It is also important that the array is quite transparent for $\gamma$ -radiation.

In the full configuration, EUCLIDES is made up of 40 two-stage ΔE-E telescopes arranged in a convex polyhedron with 42 faces, 30 hexagons and 12 pentagons. Two pentagonal faces are left empty for the incoming and outgoing beam ports. The high granularity and the $\sim$ 80% of $4\pi$ sr solid angle coverage of the complete Si-ball EUCLIDES array are able to ensure a high efficiency (60% for protons and 35% for $\alpha$ particles). The most forward part is composed of 5 hexagonal telescopes electrically segmented in 4 sectors, with equal geometrical area, to sustain a higher counting rate. The surface of each telescope is $\sim$10 cm$^2$. The silicon thickness is $\sim$100 $\mu$m and $\sim$1000 $\mu$m for ΔE and E layers respectively, which are separated by a 100 $\mu$m kapton spacer. Each telescope is placed at distances $\sim$ 6.5 cm from the target position.

Considering the fact that the reaction kinematics of a typical fusion-evaporation reaction ($v/c \approx 5\%$) are forward focused, the most forward positioned telescopes have the highest among the others counting rate. Thus, in the plunger configuration, which is the case of this experiment, in order to leave the space for the plunger installation, the backward positioned Si-telescopes which contribute negligibly to the overall detection efficiency were dismounted. Only the forward 5 segmented and 10 unsegmented ΔE-E Si telescopes were employed. The photograph of the EUCLIDES detector and the diagram of EUCLIDES coupled with the plunger device in the vacuum reaction chamber in this experiment are shown in Fig. 3.6.

The ΔE-E Si telescopes of EUCLIDES are comprised of two bulks of silicon, a

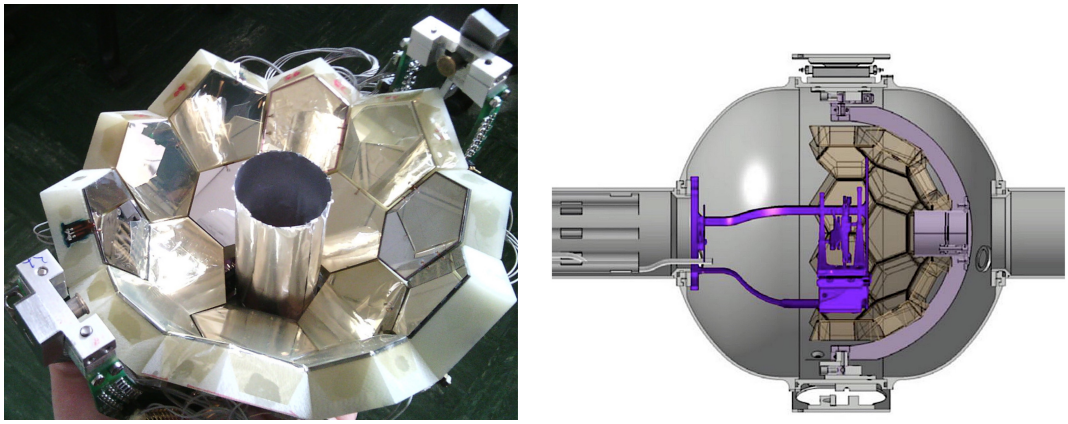

**Figure 3.6:** Left: Photograph of EUCLIDES Si-telescope array employed in this experiment. Right: The forward hemisphere of the EUCLIDES detector array (in beige/light gray) coupled with the plunger device (in dark purple) in the vacuum reaction chamber situated at the centre of GALILEO. The beam is coming from the left. Figure taken from References [24, 25].

thinner layer which allows the particle to pass through, named the ΔE detector, and a thick enough layer which is intended to completely stop particles, named the E detector. The ΔE-E technique, based on the measurement of the energy loss in the ΔE detector combined with the residual energy in the E detector, allows the light charged particles identification. The energy loss of charged ions in matter $dE/dx$, which is also known as the stopping power, can be described using the Bethe-Bloch equation [33]. If we consider a single medium (silicon for the ΔE detector), in the non relativistic case (recoil velocities $\beta$ = 3%-4%), a simple relation can be obtained:

$$\frac{dE}{dx} \propto \frac{mZ^2}{E} \tag{3.1}$$

where $E$, $m$ and $Z$ refer to the incident energy, mass and atomic number of the light charged particle passing through the thinner silicon layer, $x$ is the path length. With the recorded particle spectrum of the energy loss $dE/dx$ versus the residual energy $E$, the events corresponding to protons, deuterons and alpha particles can be clearly distinguished among different loci, each of which corresponds to

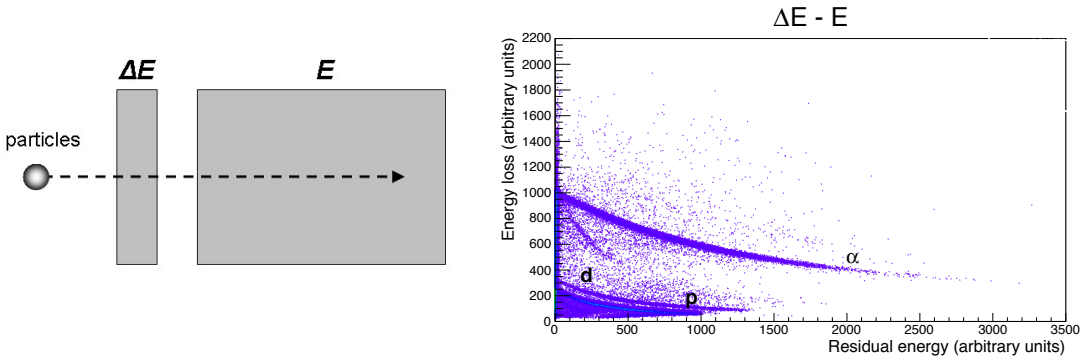


**Figure 3.7:** (Left) a schematic illustration of ΔE-E EUCLIDES telescope. (Right) the ΔE-E plot for light charged particles identification. Figure taken from [34].

different values of $mZ^2$.

Fig. 3.7 shows a schematic picture of a two-stage ΔE-E EUCLIDES telescope and a plot of the energy loss ΔE versus the residual energy E that allows to identify the light charged particles. The events corresponding to protons, deuterons and alpha particles can be well separated and clearly distinguished.

## 3.4 A dedicated plunger device for GALILEO

In order to measure the lifetimes of interest in the range from few up to several hundreds of picoseconds, the Recoil Distance Doppler-Shift (RDDS) method was employed using the plunger device. The main principle of is to have a target where the reaction or coulomb excitation takes place, and then a stopper or degrader some distance from the target in the direction of the beam [33].

The new dedicated plunger device for the GALILEO spectrometer has been developed in collaboration with the Cologne Institut für Kernphysik (IKP), with the purpose to overcome several constrains [35]:

- the possibility to vary the target-stopper distance from a few micrometers to some tens of millimeters, with sub-micrometric precision;

- the $\gamma$-rays and particles transparency of the device in order to maximize the geometrical efficiency of the apparatus;
- an active feedback system to compensate distance fluctuation between the target and stopper induced by the beam interaction with the two foils.
- the coupling with ancillary detectors, such as EUCLIDES, should be in a compact configuration to fit inside the vacuum reaction chamber of the GALILEO array.

The final design of the GALILEO plunger device is presented in Fig. 3.8. This dedicated plunger device was installed at the target position in the reaction chamber of GALILEO, holding two stretched metal foils in the beam path for the use of the recoil distance. A very compact configuration where a 24 mm $\times$ 33 mm $\times$ 20 mm motor is directly placed below the target and the stopper foils ensures a good geometrical efficiency for all GALILEO HPGe detectors except one detector located at 90° with respect to the beam axis, however the 90° ring is not usable for RDDS measurements. This LPS-24 Piezo motor, constructed by Physik Instrumente, allows the target to be moved relative to the stopper along a sliding rail, with a sub-micrometric precision ($\sim$40 nm). A good maximum displacement of around 15 mm ensures the RDDS measurement of lifetimes from a few to several hundred picoseconds.

The stretching of the target and stopper foils is implemented manually using stretcher cones. The parallelism of the two foils, which is of key importance for the precision of the distance measurement, is ensured by three screws on the target and stopper stretcher cones. The capacitance between the two foils is measured throughout the duration of the experiment and the distance fluctuation between the target and stopper is compensated by an active feedback system.

In this experiment, a 1 mg/cm$^2$ thick $^{58}$Ni target foil and a 16 mg/cm$^2$-thick $^{197}$Au stopper foil were mounted in the plunger device. The compact mechanical design allows one to combine EUCLIDES with the plunger device inside the target

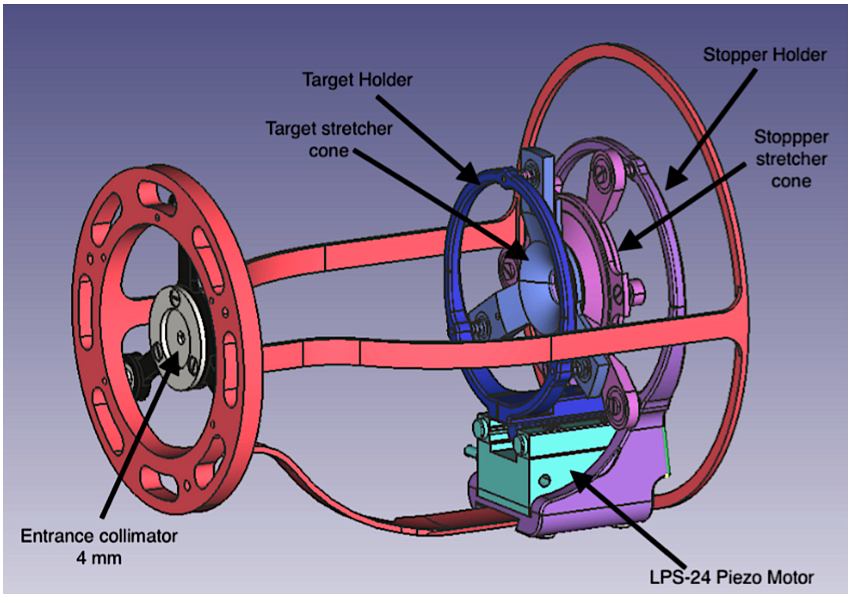


**Figure 3.8:** 3D visualisation of the GALILEO plunger device. The target and its support (in blue) and are directly mounted on the motor (in green), the position of the stopper and its support (in purple) can be varied with respect to the target. The mechanical support (in red) is fixed on the reaction chamber. Figure taken from Reference [35].

chamber and get the maximum transparency for $\gamma$-rays as well as particles. In order to measure the lifetimes of interest, the target-stopper distance was varied within a range of 10–8000 $\mu$m and the data were taken at 11 distances: 10, 17, 25, 33, 42, 100, 200, 450, 2000, 4000 and 8000 $\mu$m. The performances of the GALILEO plunger in the present experiment will be presented in Chapter 3.

# Chapter 4

# Lifetime Measurement Methodology

Different methods for lifetime measurements, covering a wide range of nuclear lifetimes ($10^{-15}$ - $10^{-5}$ s), have been developed in the past century. In Fig. 2.4 there are some methods covering different temporal ranges [23]. Since lifetimes of excited states of the $^{105}$In and $^{104}$Cd isotopes are in the ps-range, the Recoil Distance Doppler Shift (RDDS) method was applied in this work. In this chapter we focus on the description of output channel selection and the Recoil Distance Doppler Shift method (RDDS) used in this work.

## 4.1 Selection of the channel of interest

Since in a fusion-evaporation reaction various species are produced in different evaporation channels, the selection of the channel of interest can be achieved by simultaneous detection of evaporated light particles ($\alpha$, proton, deuteron, etc.) and emitted $\gamma$-rays. Conditions such as requesting $\gamma - \gamma$ coincidence with $p$, $2p$, $\alpha$, etc. can be imposed to select the reaction channels. Meanwhile, suppression of the Coulomb excitation events, due to the interaction between the $^{50}$Cr beam and the $^{197}$Au stopper could also be achieved through the selection with the detector

of light charged particles.

During the experiment, the data were collected by requiring the condition that at least one $\gamma$ ray and one particle had to be detected by GALILEO and EUCLIDES, respectively, within a time window that is shorter than the rate at which particles arrive at the target. Since all of the data is timestamped registered, events which occur in coincidence must be due to the same reaction [33].

Usually the coincidences between charged particles and $\gamma$-rays multiplicity are contaminated by channels with higher particle multiplicity. As an example, in this work, higher multiplicity channels where two or more protons were evaporated could be obtained in the $2p$-coincidencde gamma spectrum, as shown in Table 4.1.

In our experiment data, the output channel has been given as the Particle Identity (PID), the first and second digits of this notation correspond to the number of protons and $\alpha$ particles evaporated in reaching a certain channel.

| Isotope | Channel | PID ($p$,$\alpha$) |
|---|---|---|
| $^{105}$Sn | $2p1n$ | 20 |
| $^{105}$In | $3p$ | 30 |
| $^{103}$In | $3p2n$ | 30 |
| $^{104}$Cd | $4p$ | 40 |
| $^{102}$Cd | $2p1\alpha$ | 21 |

**Table 4.1:** Different output channels with $2p$ gate for the reaction between 180 MeV $^{50}$Cr beam and $^{58}$Ni target.

The complete gamma spectra in coincidencde with two protons from the preliminary analysis of our experiment are shown in Fig. 4.1 (bottom). These spectra were recorded using GALILEO $\gamma$-spectrometer in coincidence with EUCLIDES for the $^{50}$Cr (180 MeV)+$^{58}$Ni reaction.

At the chosen beam energies, there were several strongest reaction channels observed from the $2p$-coincidencde gamma spectrum: $^{50}$Cr($^{58}$Ni, $3p$)$^{105}$In, $^{50}$Cr($^{58}$Ni, $4p$)$^{104}$Cd, $^{50}$Cr($^{58}$Ni, $2p1n$)$^{105}$Sn and $^{50}$Cr($^{58}$Ni, $2p1\alpha$)$^{102}$Cd populated in the reaction. The main transitions identified for the $^{105}$In, $^{105}$Sn, $^{104}$Cd and $^{102}$Cd isotopes in the coincidence spectrum were reported in Fig. 4.1 (bottom). In particular, the transitions for different isotopes were colour marked as reported in the legend.

In view of a further channel selection, a big gain in the contaminants suppression can be achieved by gating on a transition of the isotope of interest. As the example shown in Fig. 4.1 (top), by gating on the $2p$- coincidence $\gamma$-$\gamma$ matrix on the 272 keV $19/2^+ \rightarrow 17/2^+$ transition of $^{105}$In, contaminants populated by the other reaction channels were significantly reduced.

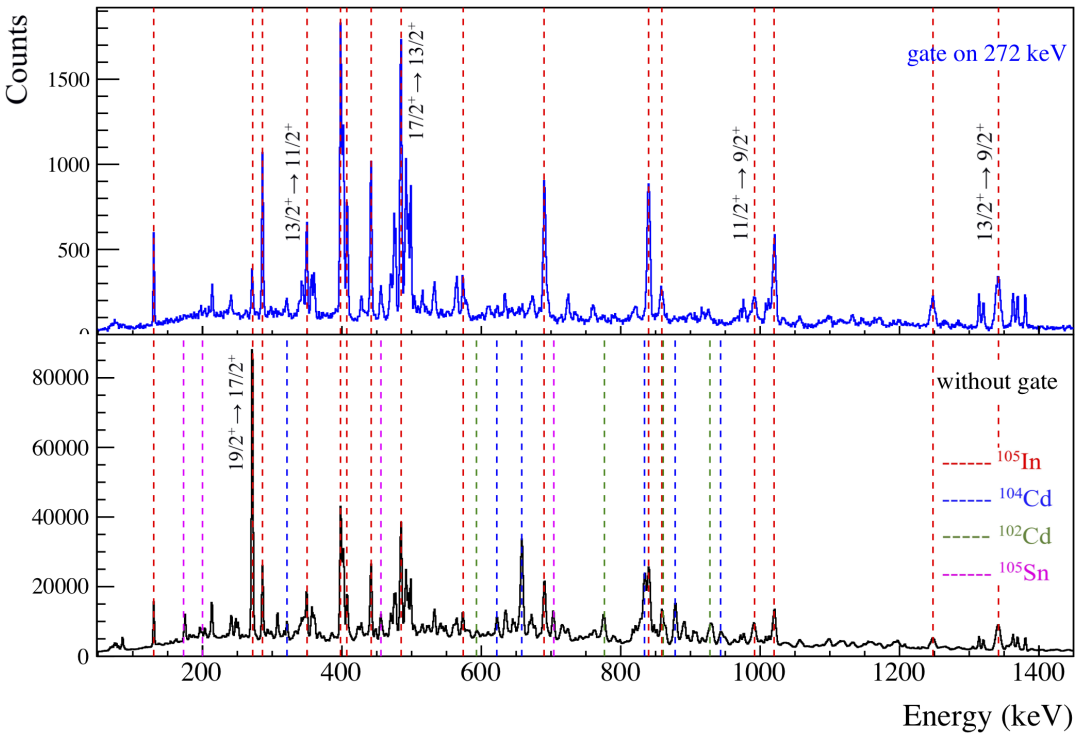


**Figure 4.1:** Total doppler corrected $2p$ $\gamma$-$\gamma$ coincidencde spectrum recorded by the 5 rings of GALILEO at a plunger distance of 4000 $\mu$m, showing the main transitions identified for the $^{105}$In, $^{105}$Sn, $^{104}$Cd and $^{102}$Cd (colour marked as reported in the legend) isotopes.

The levels below the very long-lived 1826 keV $17/2^+$ state are much shorter lived, so they will mainly have the lifetime of the $17/2^+$ level , as it is indicated by the Bateman equation. Consequently, as shown in the gated doppler-corrected spectrum in Fig. 4.1 (top), stopped components exhibit around the 485, 350, 992 and 1342 keV lines. Further, since the position of the stopped component varies for different ring angles, "satellite" peaks were observed around these four transition lines.

## 4.2 Recoil distance doppler shift method

The Recoil Distance Doppler-Shift (RDDS) method is a versatile tool in nuclear $\gamma$ spectroscopy to determine level lifetimes in the range of 1 ps to 1 ns, therefore, the absolute transition probabilities. The very attractive feature of the method is that the level lifetimes are determined directly from quantities which can be measured in an in-beam experiment. No further theories or nuclear models have to be applied. As it has previously been discussed in Chapter 2, a plunger device, which holds a fixed thin target and a movable thick stopper perpendicular to the beam path, was used to keep the recoil distance at the desired value.

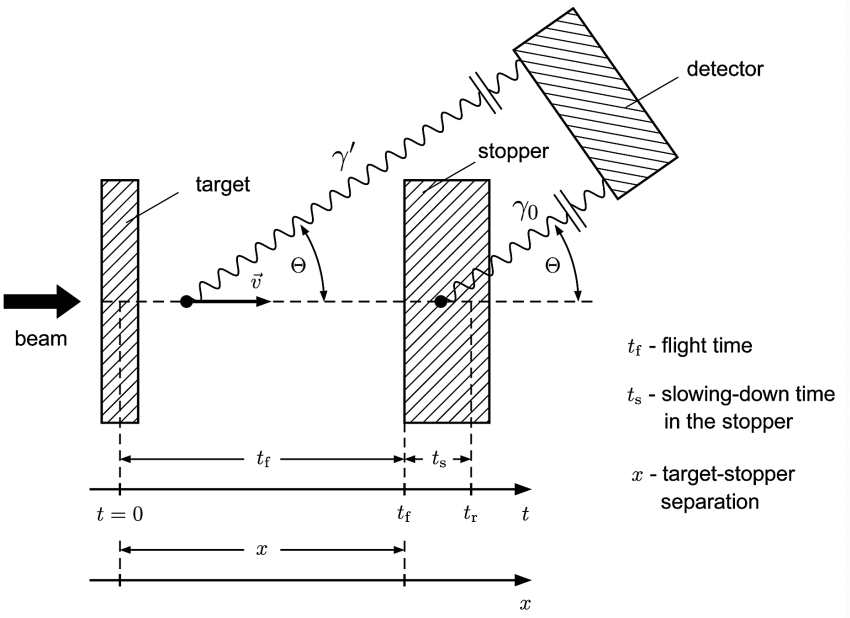


**Figure 4.2:** Schematic description of the Recoil Distance Doppler-Shift method employing the plunger device. Figure adapted from [36].

The Recoil Distance Doppler-Shift (RDDS) method is schematically illustrated in Fig. 4.2. The excited nuclear state of interest is produced by a beam-induced fusion-evaporation reaction in the target at time $t = 0$. Due to the momentum transferred from the incident particle, the recoil nucleus leaves the target with a velocity $v$ and is stopped after a flight time $t_f = x/v$ in a stopper foil, where $x$ is the separation between target and stopper. A detector is positioned at an angle $\theta$

with respect to the beam axis.

The Doppler-shifted energy is given by Equation 4.1.

$$E' = E_0 \cdot \frac{\sqrt{1-\beta^2}}{1-\beta\cos\theta} \tag{4.1}$$

with $\beta = v/c$, $c$ is the speed of light in vacuum and $\theta$ is the angle of the germanium detector with respect to the beam line. $E_0$ is the true energy of the emitted $\gamma$-ray without doppler shift. The higher recoil velocity allows a better resolution of the unshifted and shifted peaks.

The excited recoil nucleus will decay via $\gamma$-ray emission with three possible observations in the measured gamma spectra:

- $\tau \gg t_f$, the recoil will decay in the stopper, and the true energy $E_0$ will be detected.
- $\tau \ll t_f$, for each of the five rings a different Doppler-shifted energy given by Equation 4.1 is observed.
- Between the two extremes the region of sensitivity was found, where some of the recoil decay in flight and some decay in the stopper, both shifted and unshifted components of the transition can be observed, as illustrated in Fig. 4.3.

Fig. 4.3 shows the identification of the two components of the 484.7 keV $17/2^+ \rightarrow 13/2^+$ transition for all the GALILEO rings at three different target-stopper distances. The spectra are obtained by gating on the shifted component of the feeding 272 keV $19/2^+ \rightarrow 17/2^+$ transition, in a $2p$-coincidencde $\gamma - \gamma$ matrices. It was shown that the position of the in-flight component varies for the five rings, which can be indicated with e.q. 4.1, while the stopped peaks overlap.

For the analysis of the singles or coincidence plunger data, two methods have been developed which we call the conventional Decay Curve Method (DCM) and the Differential Decay Curve Method (DDCM). The coincidence technique performed

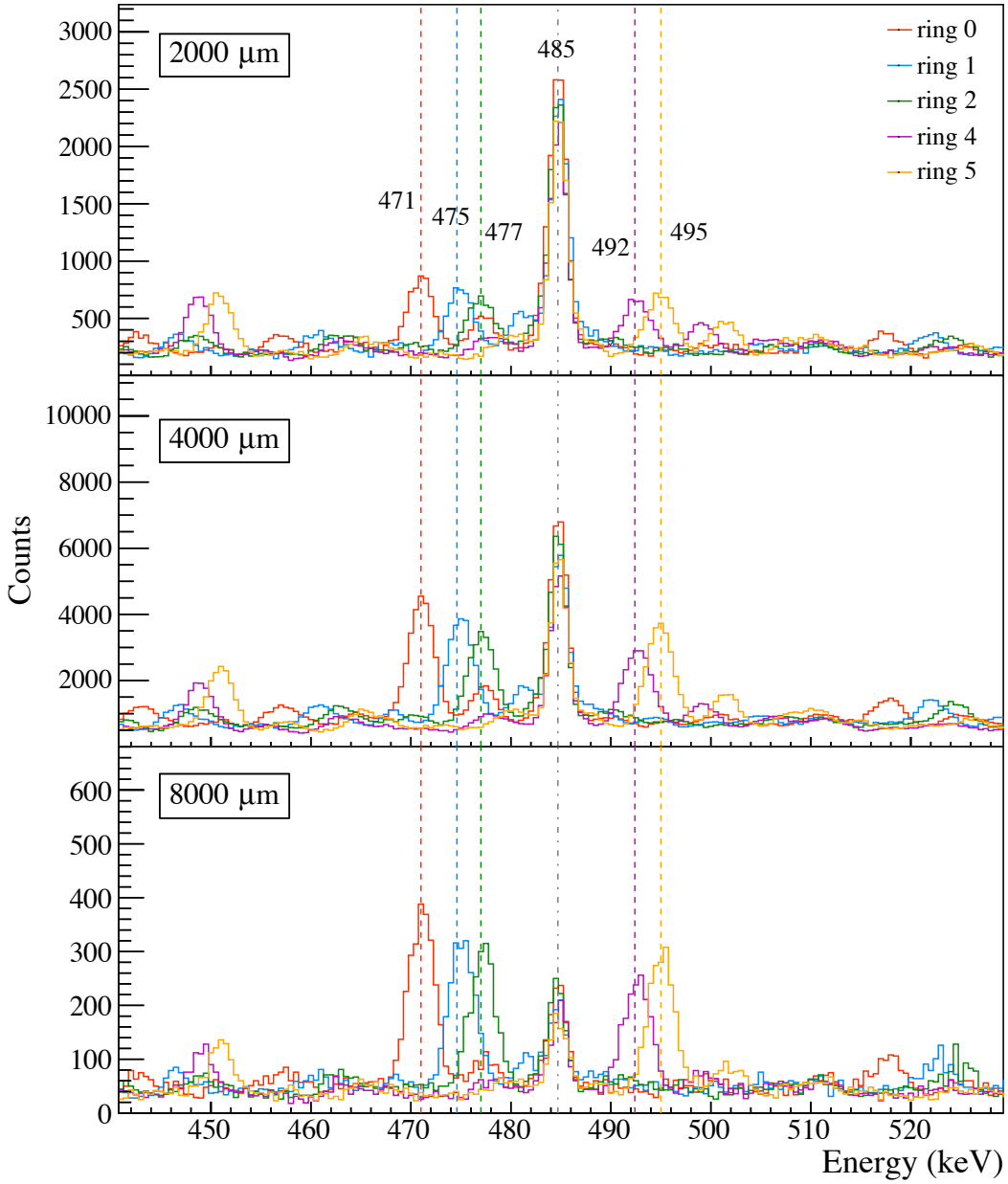


**Figure 4.3:** Partial $\gamma$ spectra showing all the different doppler shifted components for each GALILEO rings and the stopped one in the center of the 485 keV $17/2^+ \rightarrow 13/2^+$ transition of $^{105}$In in coincidence with $2p$, at plunger distances of 2000, 4000 and 8000 $\mu$m. The 485 keV transition (grey dash line), as well as shifted components at 471, 475, 477, 492 and 495 keV measured by the rings at 152°, 129°, 119°, 61°, and 51°, respectively (dot lines with color marked as reported in the legend) are shown.

with DCM and DDCM can eliminate the systematic errors usually introduced in RDDS-singles measurements by the unknown feeding history from states that lie higher in energy.

### 4.2.1 Decay Curve Method

The Decay Curve Method (DCM) is based on the extrapolation of the lifetime by observing the intensity of both shifted $I_s(x)$ and unshifted $I_u(x)$ components of a $\gamma$-ray transition as a function of the target-stopper distance $x$. As can be noticed from Fig. 4.3, for the target-stopper distances in the sensitive region, the ratio between the intensity of the unshifted and shifted components decreases with increasing target-stopper distance, i.e. the time of flight of the recoil. In particular, two ratios can be defined, the decay curve $R(x)$ and the flight curve $F(x)$

$$R(x) = \frac{I_u(x)}{I_u(x) + I_s(x)} \tag{4.2}$$

$$F(x) = \frac{I_s(x)}{I_u(x) + I_s(x)} \tag{4.3}$$

For the case of one excited level, the decay curve takes the form of an exponential, which can be related to the lifetime $\tau$ via the relationship

$$R(x) = n(0)e^{(-t/\tau)} = n(0)e^{(-\frac{x}{\beta c\tau})} \tag{4.4}$$

where $n(0)$ is the initial level population. $\beta = v/c$ has been introduced to rewrite the equation in terms of the target-stopper distance $x$, since this is how data is taken in plunger experiments, $v$ is the velocity of the recoil particle. However, a level of interest which is populated by not one but many feeding transitions is often the case, as shown in Fig. 4.4.

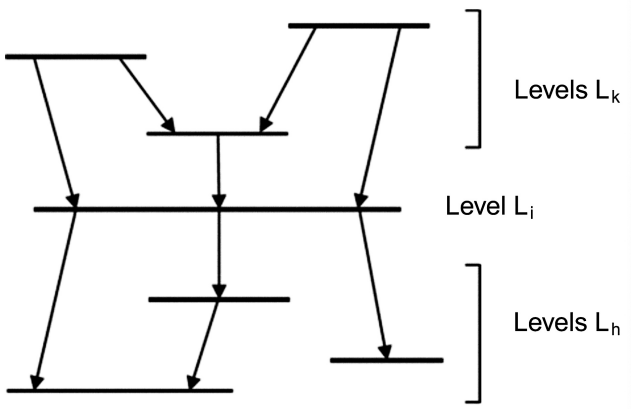


**Figure 4.4:** Schematic energy spectrum of a possible level-feeding pattern. The level of interest $i$ is fed by N transitions from the levels $k$ and deexcites via transitions to the levels $h$ ($h < i < k$). Taken from Reference [36]

This complicated level-feeding pattern gives rise to the differential equation for the level of interest $i$ reads [36]

$$\frac{d}{dt}n_i(t) = -\lambda_i n_i(t) + \sum_{k=i+1}^{N} \lambda_k n_k(t) b_{ki} \tag{4.5}$$

where $n_j(t)$ and $\lambda_j = 1 \,/\, \tau_j$ are the population at the time $t$ and decay constant of the $j$-th state, respectively. The quantity $b_{ki}$ is the branching ratio from the level $k$ to the level $i$ ($b_{ki} \neq 0$ when $i < k$). In the simple case of a decay chain when every state has just one feeder ,$b_{ki} = 1$. The solution of the differential equation with respect to the decay curve then reads

$$R_i(t) = P_i e^{-t\lambda_i} + \sum_{k=i+1}^{N} M_{ki}[(\frac{\lambda_i}{\lambda_k})e^{-t\lambda_k} - e^{-t\lambda_i}] \tag{4.6}$$

where $P_i$ denotes the direct feeding intensity of the level $i$.

Usually, the function $R_i(t)$ is fitted to the experimental data in order to determine the level lifetime $\tau_i$. Nevertheless, complementary problem can arise from the side-feeding.

### 4.2.2 Differential Decay Curve Method

The Differential Decay Curve Method (DDCM) is a transparent approach developed for the analysis of RDDS data measured as singles or as $\gamma\gamma$-coincidences.

The DDCM specific parts of the analysis include as follows [36]:

1. Finding good gates, producing gated coincidence spectra.
2. Determination of intensities for DDCM lifetime analysis.
3. Distance normalization.
4. Determination of recoil velocity.
5. Decay curves, lifetime analysis.

For the singles case analyzed by DDCM, beginning with the differential equation Eq. 4.5. After integrating, the equation for the lifetime of level $i$ can be obtained

$$\tau_i(t) = \frac{1}{\lambda_i} = \frac{-R_i(t) + \sum_{k=i+1}^{N} b_{ki}\alpha_{ki}R_k(t)}{\frac{d}{dt}R_i(t)} \tag{4.7}$$

with the factor of proportionality

$$\alpha_{ki} = \frac{\omega_k(\theta)\cdot\epsilon(E_{\gamma^k})}{\omega_i(\theta)\cdot\epsilon(E_{\gamma^i})} \tag{4.8}$$

which is determined by the detector efficiency $\epsilon(E_{\gamma^j})$ and the angular distribution $\omega_i(\theta)$ of the electromagnetic radiation.

### 4.2.3 The coincidence DDCM and DCM

#### The coincidence DDCM

A big progress in the field of lifetime measurements was achieved when the step from $\gamma$-ray singles plunger measurements to $\gamma\gamma$-coincidence measurements was made. By gating on a feeding transition B of the level of interest (see Fig. 4.5(a))

the side-feeding is eliminated and only the feeding via the transition B is relevant for the determination of the level lifetime $\tau$.

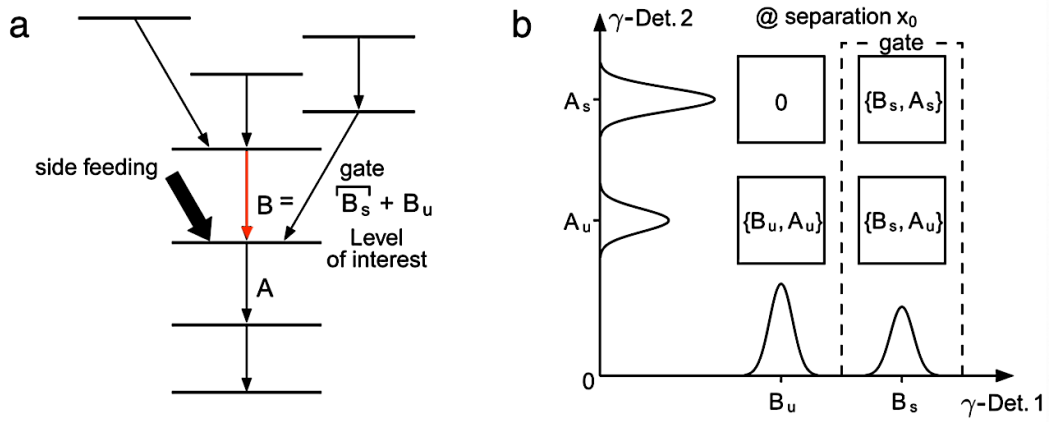


**Figure 4.5:** (a) Hypothetical level scheme. The difference between the sum of the intensities of all known depopulating transitions and the corresponding sum of all populating $\gamma$ rays was considered as sidefeeding; (b)Schematic drawing of the cascade seletion with feeding only via B in the coincidence measurement. The gate is performed on the in-flight component $B_s$ of the feeder and then the in-flight $A_s$ and the stopped $A_u$ components of the transition are observed. Figure adopted from [36].

In particular, as shown in Fig. 4.5(b), when gating on the shifted component $B_s$ of the feeding transition, two components of the depopulating transition are present: the shifted $\{B_s, A_s\}(x)$ and the stopped $\{B_s, A_u\}(x)$; on the other hand, when gating on the stopped component $B_u$ of the populating transition, only the stopped component of the depopulating transition $\{B_u, A_u\}(x)$ is present. Indeed, there cannot be an in-flight component of the transition A if the transition B happens with the nucleus at rest. Moreover, the coincidence gate on the shifted component of the feeding transition $B_s$ should be preferentially set to avoid an overestimation of the $A_u$ component due to the possible excitation of the beam ions on the stopper material, which will introduce a systematic error that leads to an overestimation of the lifetime.

It has been analytically shown that the lifetime of the level of interest derived via the coincidence DDCM is not affected by the recoil deorientation provided the

gates are set on a direct feeding transition [37]. In this particular gating case , the lifetime of state $i$ can be determined with the following formula[36]:

$$\tau_i(x) = \frac{\{B_s, A_u\}(x)}{\frac{d}{dx}\{B_s, A_s\}(x)} \frac{1}{v} \tag{4.9}$$

where $v$ denotes the recoil velocity and the quantities $\{B_s, A_u\}(x)$ and $\{B_s, A_s\}(x)$ stand for the normalized intensities of the unshifted (u) and shifted (s) component of a depopulating transition A in coincidence with the shifted component of the populating transition B at the target-stopper distance $x$.

With the coincidence DDCM, the lifetime of a state can be deduced for each plunger distance $x$ independently from the coincidence intensities of $\gamma$ rays feeding and depopulating the level of interest, thus avoiding systematical uncertainties concerning cascade and and side feedings.

However, there are two severe limitations. First, the transitions involved have to be intense enough to provide a reasonable counting rate in the coincidence spectrum with the gate set on the Doppler-shifted component of the feeding transition. In practice, this means a restriction to the main decay sequence of the level scheme. In addition, it is very important to carefully check these spectra for contaminations that unfortunately occur frequently due to the large energy widths of the gates on the shifted components and the high $\gamma$-ray density usually observed in the fusion-evaporation reaction[38].

**The coincidence DCM**

The coincidence DCM was carried out to determine effective lifetimes of weak transitions or lifetimes in cases where flight and stop peak intensities could not be analyzed individually in the spectrum. For that reason gates were set on the unshifted component of a strong low-lying transition in the decay sequence in all the rings of GALILEO at $\theta_0$=152°, $\theta_1$=129°, $\theta_2$=119°, $\theta_4$=61°and $\theta_5$=51°. The decay curve $R(x)$ function of a $\gamma$ transition depopulating the state of interest was

derived for the coincident spectrum in each "look" ring. Information about the lifetime of a state is thus determined from the shape of the decay curve fitted with analytic functions implementing the proper feeding scenario [9]. In the simplest case, where the level of interest is populated by only one feeding transition, the lifetime can be determined from the fit of a single exponential function to the $R(x)$ curve.

Besides the lifetime of the state of interest, the decay curve reflects the complete time history of the feeding of this level. To determine the lifetime, the complete feeding pattern including intensities and lifetimes has to be carefully taken into account in the analysis which is always at risk by systematical uncertainties. Despite this drawback, this way of analyzing the data is still very useful since it can be applied even to very weak transitions in the top of the cascades. Since the gating $\gamma$ ray can be chosen among all the strong transitions between low-lying states, it is nearly always possible to find a spectrum without contaminations and with enough statistics [38].

In the analysis of the plunger data, these two different methods are in a certain sense complementary. Nevertheless, with respect to the DCM analysis, especially for the ground state band, DDCM entails several advantages:

- the deduced lifetimes do not depend on the uncertainty of the absolute distance between target and stopper foils. Only the relative target-stopper distances, which can be measured with high precision in the dedicated plunger device, are required for the lifetimes investigation.
- for each state there is a certain target-stopper distance range where the data points are sensitive to the corresponding lifetime.
- there are different lifetime values estimated for each distance in the sensitive region. The final value is then a weighted average of the estimated lifetime at each distance presented, which will substantially reduce the errors.

For these reasons we can say that the coincidence DDCM provides particularly

good results in coincidence lifetime analysis for the excited states in the GSB. The analytical illustration for this conclusion is shown in Chapter 5. The DDCM as described above was used to determine most of the lifetimes for $^{105}$In and $^{104}$Cd in this work.

### 4.2.4 Distance normalization

During an RDDS experiment, the recoil production experiences fluctuations caused by a number of factors, e.g. varying measurement time at different target-stopper distances or beam current fluctuations. This means that intensities of the produced isotope of interest measured for each set distance $x$ had to be normalized. By definition, a good global normalization is valid for spectra of all angular detector rings [36].

Determination of normalization factors has to be independent from effects that result in a distance-dependent count rate for different angular rings (e.g. deorientation and solid-angle effects) and is a very sensitive part in the analysis. Errors will affect lifetimes of all nuclear levels determined from different decay curves similarly.

This was carried out for $^{105}$In by measuring the counts in both the shifted and unshifted components of the strongest $17/2^+ \rightarrow 13/2^+$ transition, with gates on both the shifted and unshifted components of the direct feeding transition $19/2^+ \rightarrow 17/2^+$. The sum of these measurements at each distance is directly proportional to the number of produced $^{105}$In nuclei at the given distance and therefore can be used to calculate a normalization factor for each distance.

### 4.2.5 Determination of the recoil velocity

Accoring to Eq. 4.1, it was possible to obtain the recoil velocity independently for each ring by a linear regression of the positions of the Doppler-shifted components of intense transitions versus unshifted $\gamma$-ray energy using the Doppler relation:

$$\beta = \frac{1}{cos\theta}(\frac{E}{E_0} - 1) \tag{4.10}$$

where $\theta$ is the angular position of the detector and $E$ and $E_0$ are the energies of the shifted and unshifted peaks. The positions of the two components of the strongest lines in $^{105}$In were determined with the Gaussian fit for the five rings of GALILEO, with gates setting on the stopped components of the strong $E2$-transitions lines of $^{105}$In to avoid contaminations [4].

In the present experiment, the weighted average recoil velocity was deduced to be $v = 9.84(60)$ $\mu$m/ps or 3.28 (20)% of the speed of light, utilized for $^{105}$In and $^{104}$Cd for all combinations of ring pairs.

# Chapter 5

# Results from Lifetime Measurements

In order to check the validity of the adopted experimental setup and plunger technique, as well as to contribute to the discussion on nuclear structure physics in the neutron deficient region close to the N = Z = 50 double-shell closure, the electromagnetic studies based on direct lifetime measurements of the excited states in the Ground State Bands (GSB) of an odd-mass In isotope $^{105}$In and an even-mass Cd isotope $^{104}$Cd have been conducted with the coincidence Recoil Distance Doppler Shift (RDDS) technique, for the reason that the excited states of $^{105}$In and $^{104}$Cd are the most strongly populated in the experiment.

The target-stopper distances covered by the dedicated plunger in the experiment were 10, 17, 25, 33, 42, 100, 200, 450, 2000, 4000 and 8000 $\mu$m. The distances in the range between 10 and 450 $\mu$m allowed the measurement of the very short lifetimes of the high-spin magnetic band, e.g. from 1 to dozens of picoseconds at the typical recoil velocity of fusion-evaporation reaction of $v = 10$ $\mu$m/ps, while the distances up to 8000 $\mu$m covered the long-lived states with lifetimes up to hundreds of picoseconds.

Level lifetimes have been determined for the $17/2^+$ up to $25/2^+$ states in the

GSB of $^{105}$In and the $2^+$, $4^+$, $11^+$ and $12^+$ states in $^{104}$Cd. The low-lying excited states of $^{104}$Cd and $^{105}$In are used as benchmark of the experimental method and analysis thanks to their large statistics in the $2p$-coincidencde $\gamma$-$\gamma$ spectra and well known lifetimes in the literature. At the end of the chapter, the feasibility of measuring lifetimes in the identified odd-mass Sn isotopes, $^{105}$Sn, is discussed.

## 5.1 Lifetimes of the nucleus $^{105}$In

The 485 keV $17/2^+ \rightarrow 13/2^+$ transition in the Ground State Band (GSB) is the strongest line of $^{105}$In observed in the reaction. In this work, therefore, the investigation began with a lifetime measurement of the long living $17/2^+$ excited state via the the coincidence DCM and DDCM. In particular a detailed discussion is focused on the comparison of the results obtained with the value adopted in literature.

The DCM was carried out using the ROOT software while the DDCM performed with the Napatau software [39], for which one provides input files containing the plunger distances, normalization factors, recoil velocity of the isotope of interest and the areas and corresponding errors of the shifted and unshifted components of a transition depopulating the level of interest. The recoil velocity $v/c$ used in Napatau in the present work was 0.0335.

In addition, lifetimes of four higher lying states above the $17/2^+$ state in the GSB were extracted via the coincidence DDCM to find out the problems that may be encountered in the lifetime analysis with low statistics.

### 5.1.1 Lifetime of the $17/2^+$ state

The lifetime investigation began with presorting of the data, namely checking gate and looking for the transition of interest via the projections of $2p$-coincidencde $\gamma$-$\gamma$ matrices with the ROOT [40] software package. The $\gamma$-$\gamma$ matrices were constructed from different ring combinations at each plunger distances.

**DDCM**

The coincidence DDCM was employed by gating on the shifted component of a directly populating transition, i.e. the 272 keV $19/2^+ \rightarrow 17/2^+$ transition, in order not to account for the feeding from higher excitation energy states. $\gamma$-$\gamma$ matrices recorded from ring $\theta_i$ in coincidence with all of the rings after Doppler correction ($\theta_i$ - $\theta_{AllDC}$, i = 0, 1, 2, 4, 5) were adopted for the DDCM investigation. $\theta_{AllDC}$ indicates that the resulting "look" spectra is the sum of the five rings after Doppler correction.

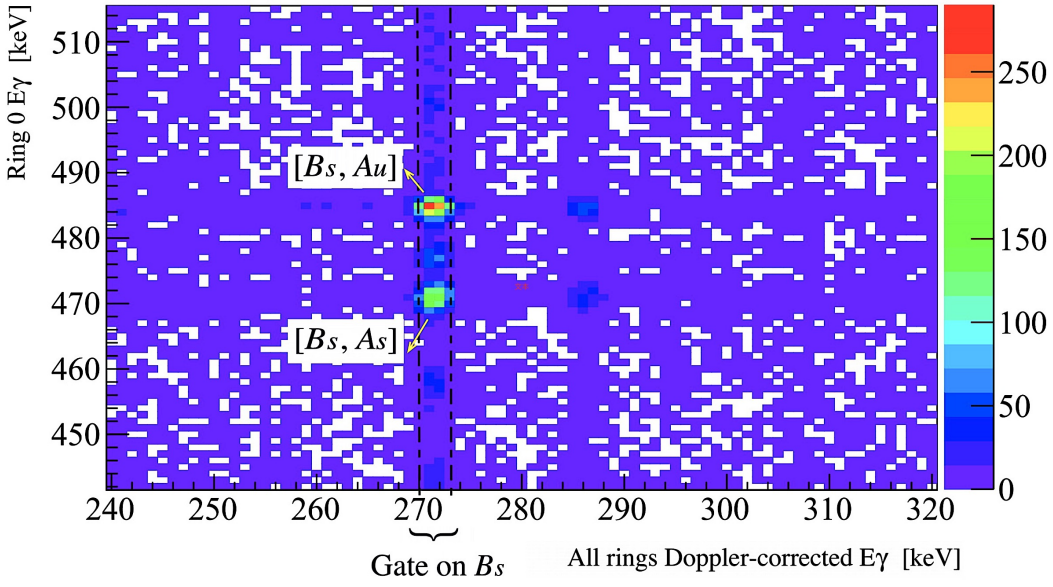


**Figure 5.1:** $2p$-coincidencde $\gamma$-$\gamma$ matrix for $^{105}$In at 4000 $\mu$m plunger distance constructed from GALILEO ring combination $\theta_0$ - $\theta_{AllDC}$, showing the locations of the shifted ($\{B_s, A_s\}$) and unshifted ($\{B_s, A_u\}$) components of the 485 keV $17/2^+ \rightarrow 13/2^+$ transition with a 3 keV gate set on the shifted ($B_s$) component of the 272 keV $19/2^+ \rightarrow 17/2^+$ transition.

The partial spectrum of the $2p$-coincidencde $\gamma$-$\gamma$ matrix at 4000 $\mu$m plunger distance constructed from combination $\theta_0$ - $\theta_{AllDC}$ is shown in Fig. 5.1. The coincidences of the shifted ($B_s$) components of the 272 keV $19/2^+ \rightarrow 17/2^+$ transition with the shifted ($A_s$) and unshifted ($A_u$) components of the 485 keV $17/2^+ \rightarrow 13/2^+$ transition are indicated on the matrix. The location of the gate has also been shown, after the Doppler correction for the abscissa, by placing a 3 keV gate at 272 keV, the coincidence gate was set on the shifted component of the $19/2^+ \rightarrow 17/2^+$ transition in each of the five rings. The statistics of the peak intensities in the gated spectra will be improved with the larger energy width of the gate, but contaminations will also occur around the weak transition of interest due to the large gates.

As an example, figure 5.2 shows the $2p$-$\gamma$-$\gamma$ coincidence spectra of the 485 keV $17/2^+ \rightarrow 13/2^+$ transition obtained through gating on the shifted component of the directly populating transition at different plunger distances. While augmenting the target-stopper distance, the intensity of the shifted component ($I_{sh}$) increase and of the unshifted component ($I_{un}$) decrease progressively.

The intensities of the shifted and unshifted components of the 485 keV $17/2^+ \rightarrow 13/2^+$ transition were determined in the projections of the $2p$-coincidencde $\gamma$-$\gamma$ matrices performed with ROOT [40]. The shifted and unshifted peaks of the state of interest in the coincident spectra were fitted with a gaussian function on top of a first order polynomial for the background. The errors of the intensities of both peaks were obtained by extracting the sub matrix of the gaussian parameters from the covariance matrix of the total fitting curve by ROOT. Figure 5.3 presents the fitting of the observed peaks in the coincident spectra constructed by $\theta_0$ - $\theta_{AllDC}$ and $\theta_5$ - $\theta_{AllDC}$ ring combinations at different plunger distances.

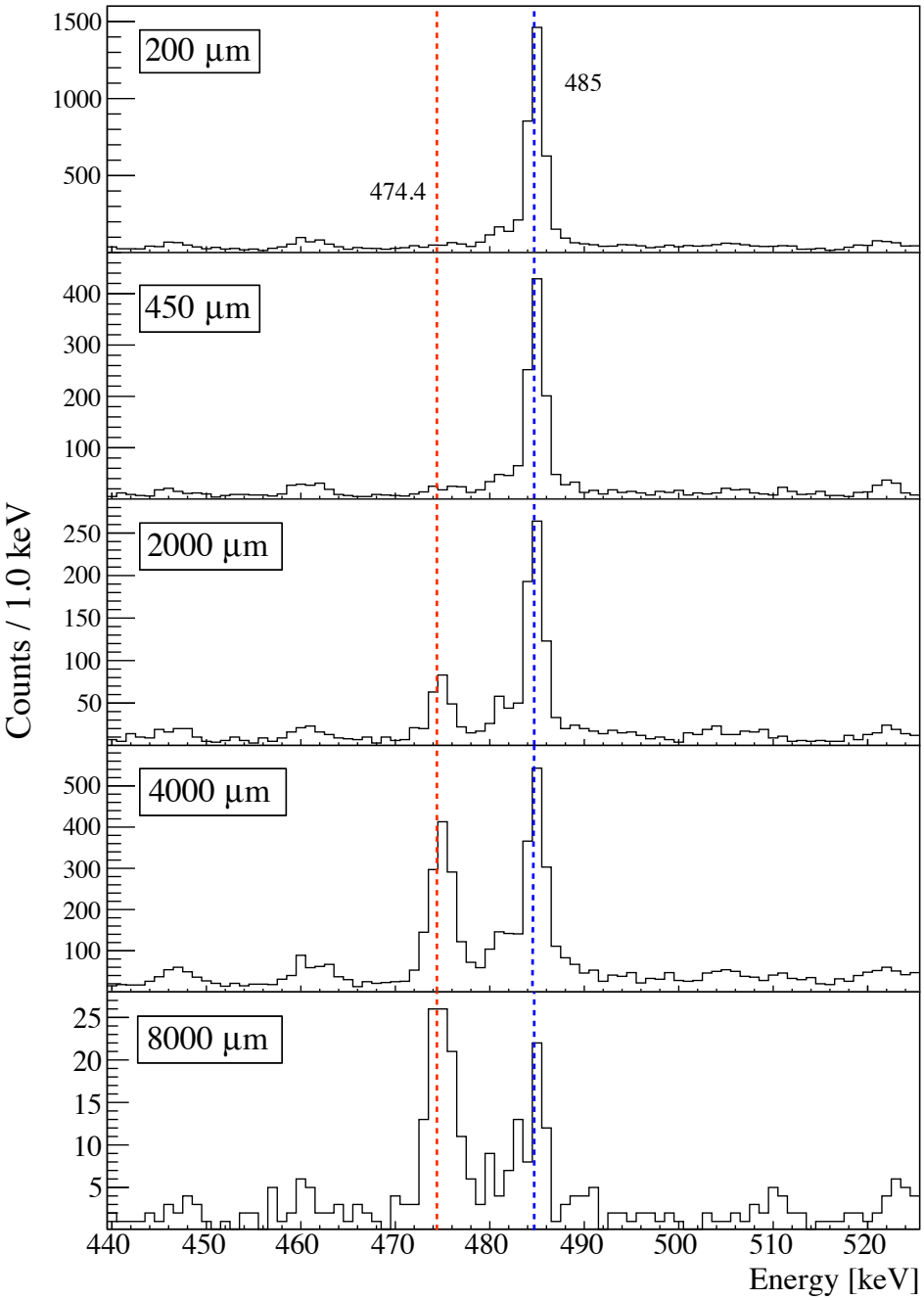


**Figure 5.2:** Partial gated $\gamma$-$\gamma$ coincidence spectra, measured by GALILEO ring combination $\theta_1$ - $\theta_{AllDC}$ for five different plunger distances, obtained by gating on the Doppler shifted component ($B_s$) of the 272 keV $19/2^+ \rightarrow 17/2^+$ transition showing the shifted ($\{B_s, A_s\}(x)$, red dot lines) and unshifted ($\{B_s, A_u\}(x)$, blue dash lines) components of the 485keV $17/2^+ \rightarrow 13/2^+$ transition in $^{105}$In.

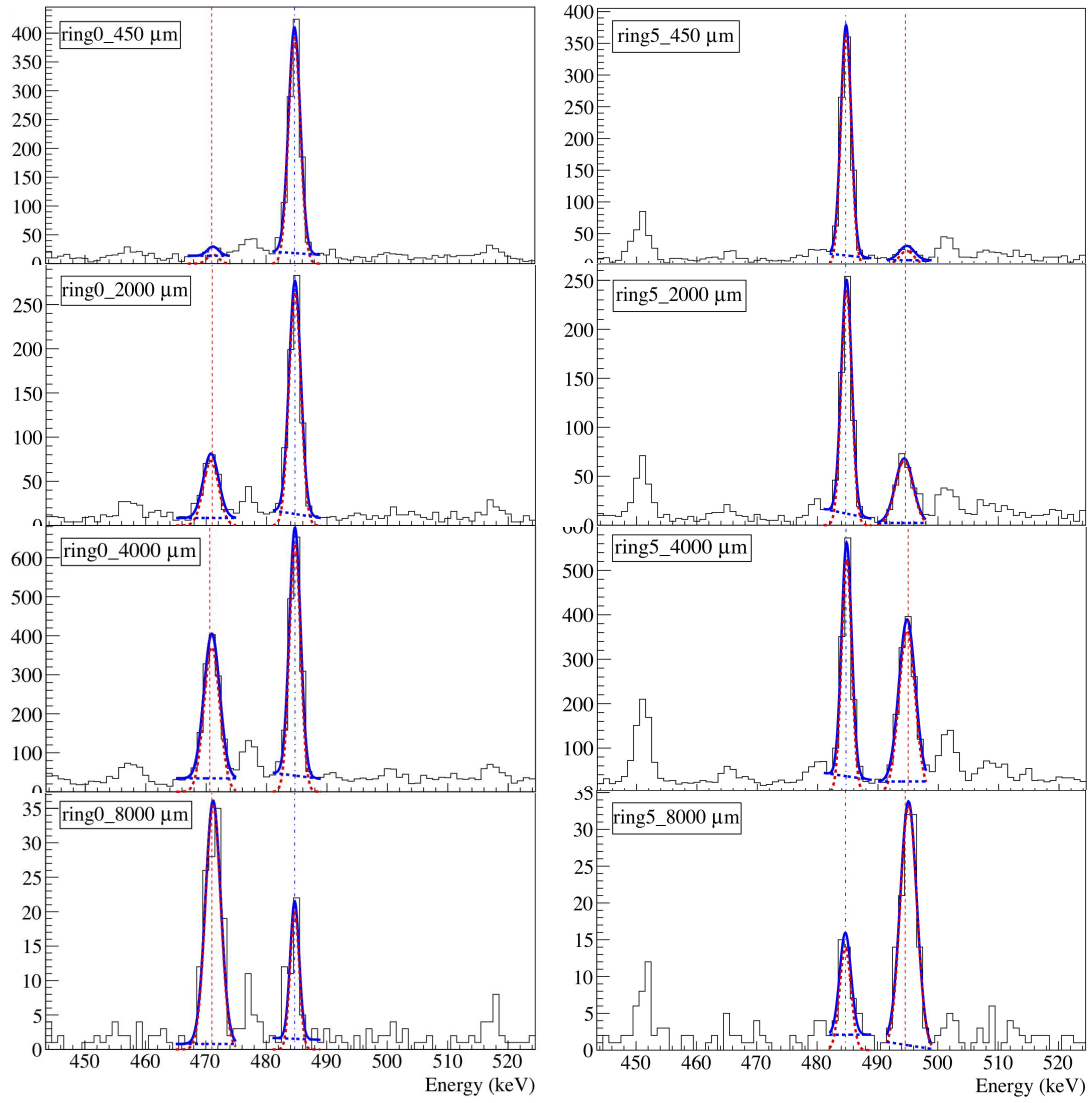


(a) $^{105}$In, 152° (b) $^{105}$In, 51°

**Figure 5.3:** Fitting of the observed peaks to extract the intensities of the shifted and unshifted components of the 485 keV $17/2^+ \rightarrow 13/2^+$ transition in $^{105}$In, performed with ROOT. Spectra (a) and (b) were constructed from GALILEO ring combinations $\theta_0$ - $\theta_{AllDC}$ and $\theta_5$ - $\theta_{AllDC}$ at 450, 2000, 4000 and 8000 $\mu$m plunger distances, respectively. Each component was fitted with a gaussian function (red dotted [peak]) on top of a first order polynimials for the background (blue dotted). The resulting curves are shown by the solid blue lines. Intensity for each component was determined after the background subtraction.

Once the peak areas have been measured after the background subtraction, the Napatau software [39] was used to implement the DDCM to obtain the lifetime. A typical analysis by Napatau for the lifetime investigation of the $17/2^+$ state from ring combination $\theta_1$ - $\theta_{AllDC}$ is illustrated in figure 5.4. The datapoints of $I_{un}$ (bottom) and $I_{sh}$ (middle) are fitted simultaneously with a few continuously-connected second-order polynomials.

According to Eq. 4.9, the derivative $itd/dx$ of the curve for the shifted component (the denominator of Eq. 4.9) multiplied by a constant should be equal to the curve of the unshifted component at the same plunger distance. This constant gives the lifetime of the state multiplied by the recoil velocity. Then the lifetime estimate can be modified to minimize the total $\chi^2$ of both fits, which has the advantage over the DCM method of fitting with just the $I_{un}/(I_{un} + I_{sh})$ ratio by effectively doubling the number of points one can use to determine a lifetime [33].

The lifetime of the state of interest can be deduced for each plunger distance $x$ independently and should sit at a constant value in the sensitivity region, where the derivative of the shifted component (the denominator of Eq. 4.9) is largest, to reduce the systematic effects. [41]. Therefore, for a certain ring combination, the weighted average $\tau_{av}$ is taken from the derived values within the sensitivity region.

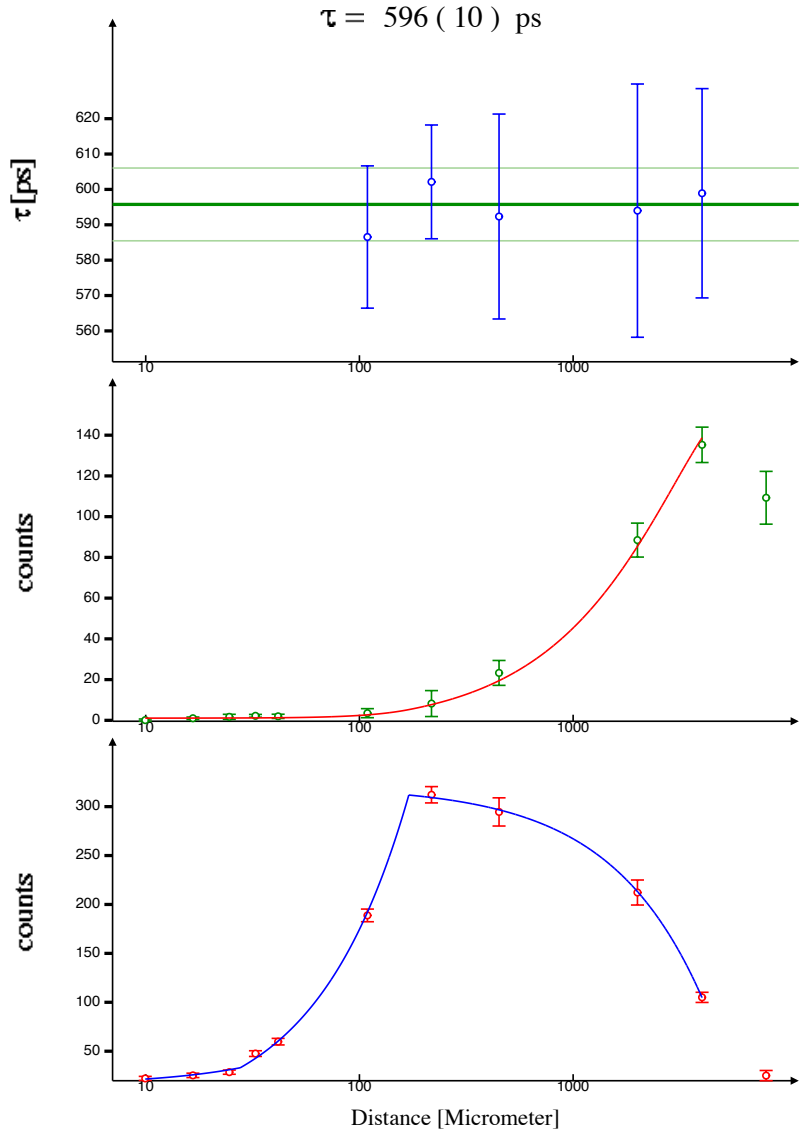


**Figure 5.4:** (Top) Lifetime values extracted at each distance in the sensitive region for the 485 keV $17/2^+ \rightarrow 13/2^+$ transition in $^{105}$In, measured at 129°, obtained via DDCM: The solid and dashed lines represent the weighted average and the associated uncertainty, respectively. (Middle) Normalized intensity curve for the shifted component, $I_{sh}$, fitted (solid line) with a function consisting of continuous, piecewise second-order polynomials. (Bottom) Normalized intensity curve for the unshifted component, $I_{un}$. The curve at the bottom is proportional to the derivative of that in the middle and both curves are fitted simultaneously.

This process was repeated independently for the five data sets corresponding to the five GALILEO ring angles of observation $\theta_{0,1,2,4,5}$=152°, 129°, 119°, 61°and

51°. The results obtained are presented in Table 5.1 along with a final weighted average, $\tau_{av} = 605(5)$ ps.

| Ring combination | $\tau_{exp}$ [ps] |
|---|---|
| $\theta_0$ - $\theta_{AllDC}$ | 605(11) |
| $\theta_1$ - $\theta_{AllDC}$ | 596(10) |
| $\theta_2$ - $\theta_{AllDC}$ | 626(12) |
| $\theta_4$ - $\theta_{AllDC}$ | 620(11) |
| $\theta_5$ - $\theta_{AllDC}$ | 579(11) |
| Weighted Average | 605(5) |

**Table 5.1:** Table of lifetime values measured for the $17/2^+$ level, obtained via the Differential Decay Curve Method.

### DCM

In the coincidence DCM analysis, to obtain lifetime information about the state of interest, decay curves were determined in coincidence with a strong low-lying transition. In order to keep the high statistics, $\gamma$-$\gamma$ matrices recorded from ring $\theta_i$ in coincidence with all of the rings ($\theta_i$ - $\theta_{All}$, i = 0, 1, 2, 4, 5) were adopted for the DCM investigation. $\theta_{All}$ indicates that the resulting "look" spectra is the sum of the five rings. As shown in Fig. 5.5, by placing a 3 keV gate at 272 keV, the coincidence gate was set for the five rings on the unshifted component of the $19/2^+ \rightarrow 17/2^+$ transition, which is the strongest transition apart from the 485 keV line (see Fig. 1.1).

The intensities $I_{sh}$ and $I_{sh}$ were determined with ROOT by fitting the experimentally observed spectra with simulated gaussian functions on top of two first order polynomials for the background. By extracting the sub matrix of the gaussian parameters from the covariance matrix of the total fitting curve, the errors of the intensities of both peaks were obtained and therefore the errors of the $I_{un}/(I_{un} + I_{sh})$ ratios were calculated with the error propagation formula. As a result, the ratios with errors as a function of the target-stopper distance, the $R(x)$

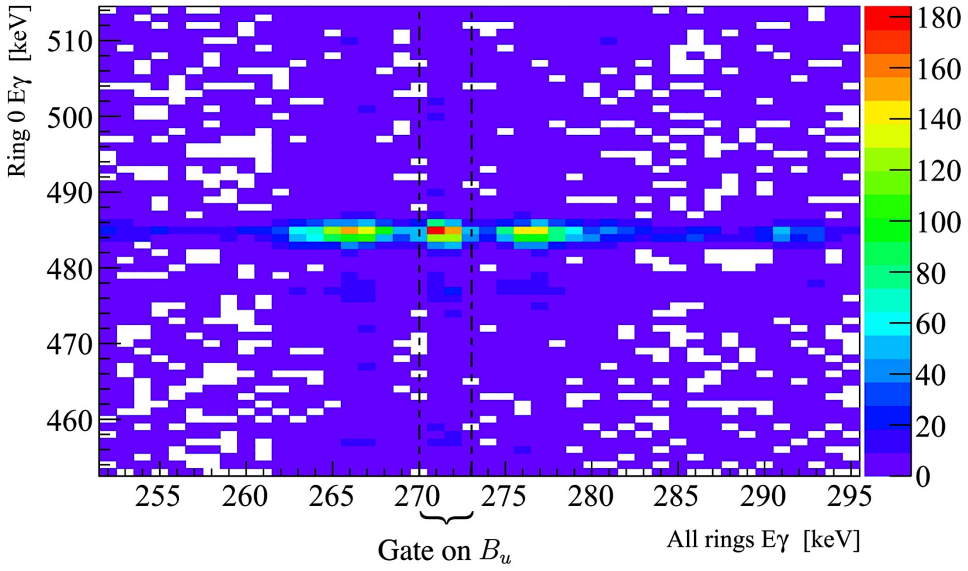


**Figure 5.5:** $2p$-coincidencde $\gamma$-$\gamma$ matrix for $^{105}$In at 100 $\mu$m plunger distance constructed from GALILEO ring combination $\theta_0$ - $\theta_{All}$, showing the locations of the shifted and unshifted components of the 485 keV $17/2^+ \rightarrow 13/2^+$ transition with a 3 keV gate set on the unshifted ($B_u$) component of the 272 keV $19/2^+ \rightarrow 17/2^+$ transition.

curve, can be obtained.

According to Equation 4.4, the effective lifetime for the 1826 keV $17/2^+$ state of $^{105}$In was extracted by a fit of a single exponential function to the $R(x)$ curve. Figure 5.6 and Figure 5.7 show the decay curves extracted for $\theta_0$ - $\theta_{All}$ and $\theta_5$ - $\theta_{All}$ with the exponential fit.

The DCM was repeated for the coincidence spectra detected by five ring combinations and the measured results are presented in table 5.2 along with a weighted average 641(17) ps.

The lifetime values obtained for the $17/2^+$ level of $^{105}$In by DCM and DDCM are compatible with the value reported in literature of $T_{1/2}$ = 416(28) ps [8]. Considering that $\tau = T_{1/2}/ln2$, $\tau_{adopted}$ = 600(40) ps. The comparison between the experimental results and the value adopted in the literature is summarized in Table 5.3.

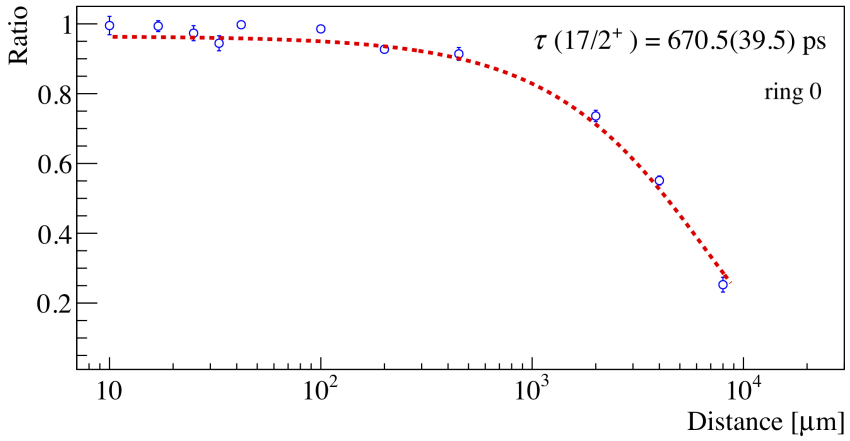


**Figure 5.6:** Lifetime of the $17/2^+$ state extracted for ring combination $\theta_0$ - $\theta_{AllDC}$ by DCM.

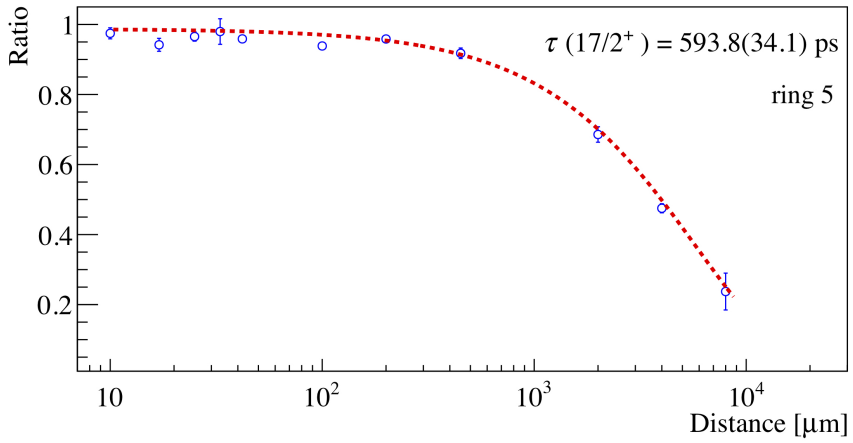


**Figure 5.7:** Lifetime of the $17/2^+$ state extracted for ring combination $\theta_5$ - $\theta_{AllDC}$ by DCM.

We confirmed the literature adopted value with substantially reduced errors, especially via DDCM. The preliminary measurements with the Recoil Distance Doppler Shift technique are very promising and demonstrated the better performance of the Differential Decay Curve Method compared to the Decay Curve Method (see Section 4.2.2) for the high intense $\gamma$ tansitions. In order to validate the experimental technique for the excited states higher up in the GSB, i.e. transition lines typically with much lower intensities, further work on the lifetime determinations of the $19/2^+$, $21/2^+$, $25/2^+$ yrast states of $^{105}$In were conducted via DDCM.

| Ring combination | $\tau_{exp}$ [ps] |
|---|---|
| $\theta_0$ - $\theta_{All}$ | 670(39) |
| $\theta_1$ - $\theta_{All}$ | 586(34) |
| $\theta_2$ - $\theta_{All}$ | 695(40) |
| $\theta_4$ - $\theta_{All}$ | 699(40) |
| $\theta_5$ - $\theta_{All}$ | 594(34) |
| Weighted Average | 641(17) |

**Table 5.2:** Table of lifetime values measured for the $17/2^+$ level, obtained via the Decay Curve Method.

| | DCM | DDCM | Literature value |
|---|---|---|---|
| $\tau$ [ps] | 641(17) | 605(5) | 600(40) |

**Table 5.3:** Table of lifetime values measured for the $17/2^+$ level, obtained via the Differential Decay Curve Method. Lifetime of the $17/2^+$ state of $^{105}$In obtained via DCM and DDCM, the results are compared to the adopted value in the nuclear data sheet [8].

### 5.1.2 Lifetime of the $19/2^+$ state

To determine the lifetime of the $19/2^+$ state at an excitation energy of 2098 keV, a gate was set on the Doppler shifted component of the 840 keV $21/2^+ \rightarrow 19/2^+$ transition (see Fig.1.1). Figure 5.8 shows the curves with unshifted and shifted intensities of the depopulating transition and the $\tau$-curve for the spectra recorded in ring combination $\theta_0$ - $\theta_{AllDC}$. The extracted values for the five rings are presented in Table 5.4, which shows the consistent results yielding a weighted average for the lifetime of 3.90(7) ps. This value agrees with the previous measurement (3.76(18) ps [8]) but is an order of magnitude more precise.

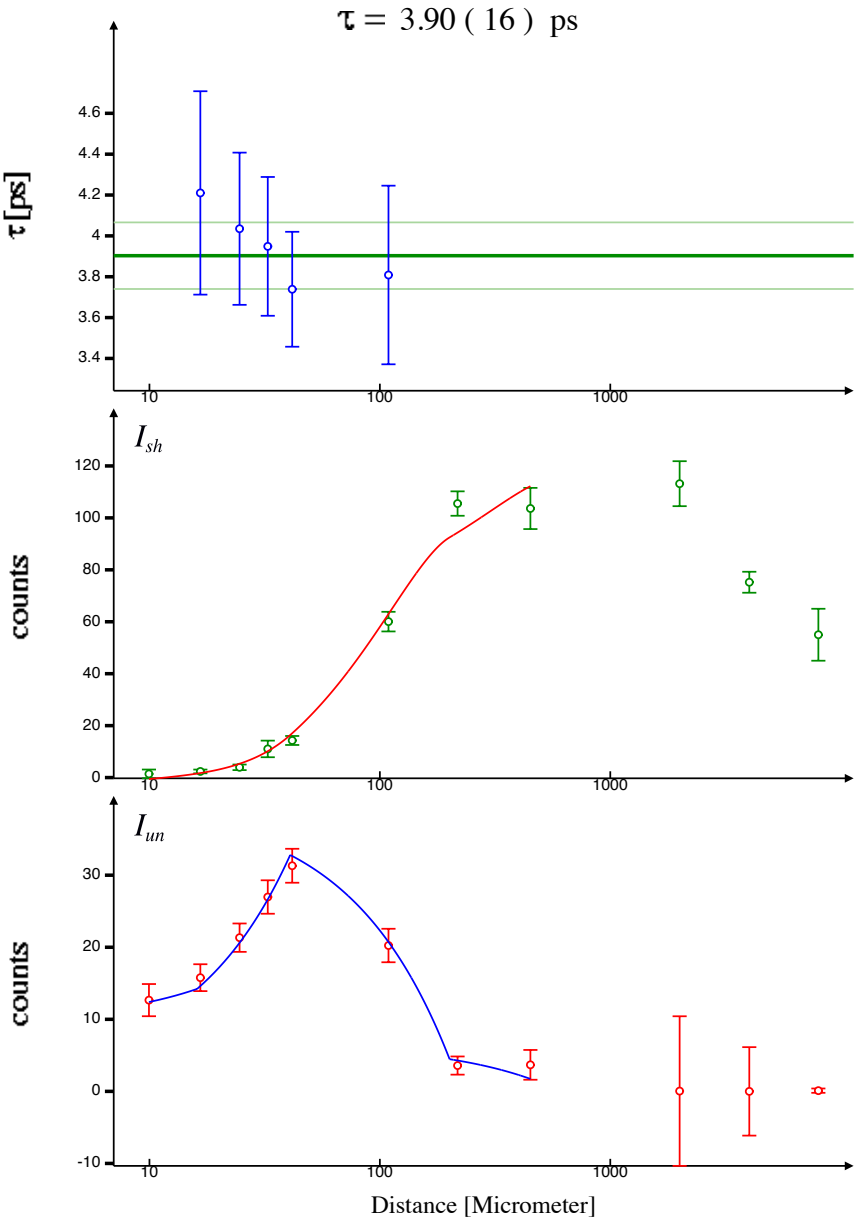


**Figure 5.8:** $\tau$-plot (Top) and intensities of the shifted $I_{sh}$ (middle) and unshifted $I_{un}$ (bottom) components of the 272 keV $19/2^+ \rightarrow 17/2^+$ transition of $^{105}$In, measured at 152°, obtained via DDCM.

| Ring combination | $\tau_{exp}$ [ps] |
|---|---|
| $\theta_0$ - $\theta_{AllDC}$ | 3.90(16) |
| $\theta_1$ - $\theta_{AllDC}$ | 3.75(16) |
| $\theta_2$ - $\theta_{AllDC}$ | 3.67(17) |
| $\theta_4$ - $\theta_{AllDC}$ | 4.22(21) |
| $\theta_5$ - $\theta_{AllDC}$ | 4.06(14) |
| Weighted Average | 3.90(7) |

**Table 5.4:** Table of lifetime values measured for the $19/2^+$ level, obtained via the DDCM.

### 5.1.3 Lifetime of the $21/2^+$ state

As the measurement moved to higher spin states, the transitions became weak and the statistics of the data began to reduce, due to the typical high number of potential $\gamma$ decay paths at higher excitation energies. In addition, as the lifetimes of the higher spin states become shorter, the number of distances which can be used to make the fit in Napatau decreases, which brings larger uncertainty in the analysis. A typical case is the $21/2^+$ state with a $< 1$ ps lifetime. The lifetime of this state was obtained by setting a gate on the shifted component of the 407 keV $23/2^+ \rightarrow 21/2^+$ transition (see Fig.1.1).

A more noticeable problem is that the Doppler shifted component of 407 keV $23/2^+ \rightarrow 21/2^+$ transition in ring 1 overlaps with the unshifted component of the $25/2^- \rightarrow 23/2^-$ transition at energy 398 keV. These overlaps therefore caused extra unshifted intensity in the $21/2^+ \rightarrow 19/2^+$ transition from ring 1 in the accumulated $\theta_i$ - $\theta_{AllDC}$ spectra, as indicated in Figure 4.5.

In principle, this problem can be avoid to analyse the $\gamma$-$\gamma$ matrices constructed from the $\theta_i$ - $\theta_j$ ring combinations rather than the accumulated $\theta_i$ - $\theta_{AllDC}$ spectra at the expense of statistics. Then the ring combinations recording extra intensities, as discussed above $\theta_i$ - $\theta_1$, can be discarded. However, this is not a solution for

low-intensity transitions considering the statistics of our experimental data.

Figure 5.9 shows the poor statistics of the peaks intensities of the depopulating transition and the limited number of distances that can be used to make the fit, resulting in the large uncertainty in the DDCM analysis.

The extracted lifetime values for different rings results are summarized in Table 5.5. Ring combination $\theta_5$ - $\theta_{AllDC}$ could not be used in the measurement since the 858.5 keV $29/2^+ \rightarrow 25/2^+$ transition overlaps with the shifted peak at 858 keV corresponding to the $21/2^+ \rightarrow 19/2^+$ transition being measured.

The lifetime determined for the level $21/2^+$ state from this work is $\tau = 0.92(5)$ ps while the value reported in literature is 0.75(15) ps extracted via DDCM in [8]. The deviation comes from the extra unshifted intensity of the directly depopulating transition due to the presence of a contaminant line at 398 keV falling under the gate in ring 1, as discussed above.

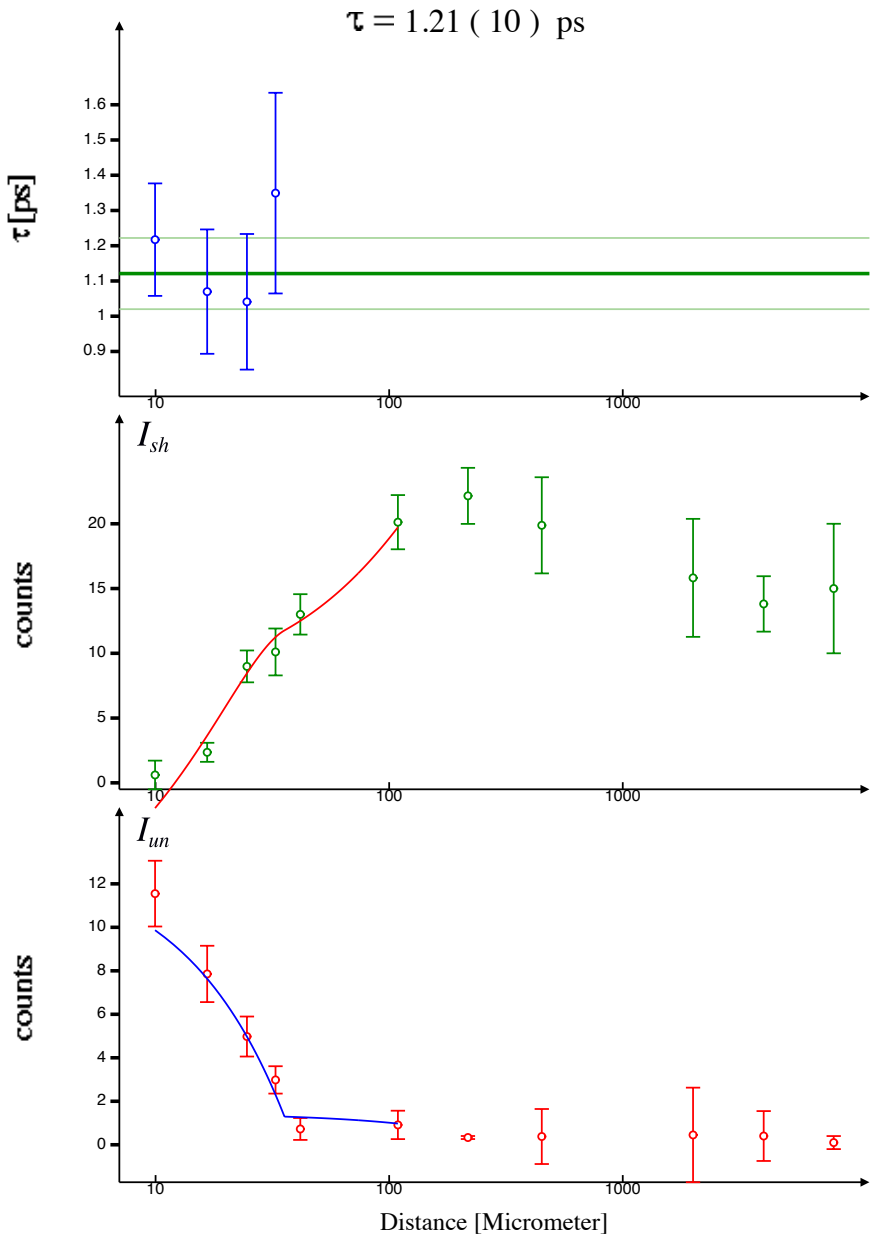


**Figure 5.9:** $\tau$-plot (Top) and intensities of the shifted $I_{sh}$ (middle) and unshifted $I_{un}$ (bottom) components of the 840 keV $21/2^+ \rightarrow 19/2^+$ transition of $^{105}$In, measured at 129°, obtained via DDCM.

| Ring combination | $\tau_{exp}$ [ps] |
|---|---|
| $\theta_0$ - $\theta_{AllDC}$ | 0.79(9) |
| $\theta_1$ - $\theta_{AllDC}$ | 1.12(9) |
| $\theta_2$ - $\theta_{AllDC}$ | 0.95(10) |
| $\theta_4$ - $\theta_{AllDC}$ | 0.87(9) |
| Weighted Average | 0.92(5) |

**Table 5.5:** Table of lifetime values measured for the $21/2^+$ level, obtained via DDCM.

### 5.1.4 Lifetime of the $23/2^+$ state

Both DDCM and DCM have been tentatively employed for the $23/2^+$ state depopulated through 407 keV $23/2^+ \rightarrow 21/2^+$ and 1248 keV $23/2^+ \rightarrow 19/2^+$ transitions (see Fig.1.1). This section presents the analytical illustration of the limitations of both methods caused by the poor statistics, contaminations and side-feeding from the unobserved populating transitions. The intensity of the side-feeding of the $23/2^+$ state has a relative intensity of 40 % of the complete feeding [9].

**DDCM**

The 1011 keV feeding transition is too weak to set gates on its shifted component. Thus for a first step, DDCM was employed by setting a 3 keV gate on the 286 keV feeding transition and very low-intensity spectra were obtained. By gating on the direct feeding transition the side-feeding is eliminated.

In the case of the depopulating 407 keV transition, a serious problem is that, within the energy range of about 400 keV, a number of contaminations due to the $\gamma$ dacays of higher levels (see Ref. [8]) of $^{105}$In occurred in the gated spectra, as indicated in Fig. 5.10.

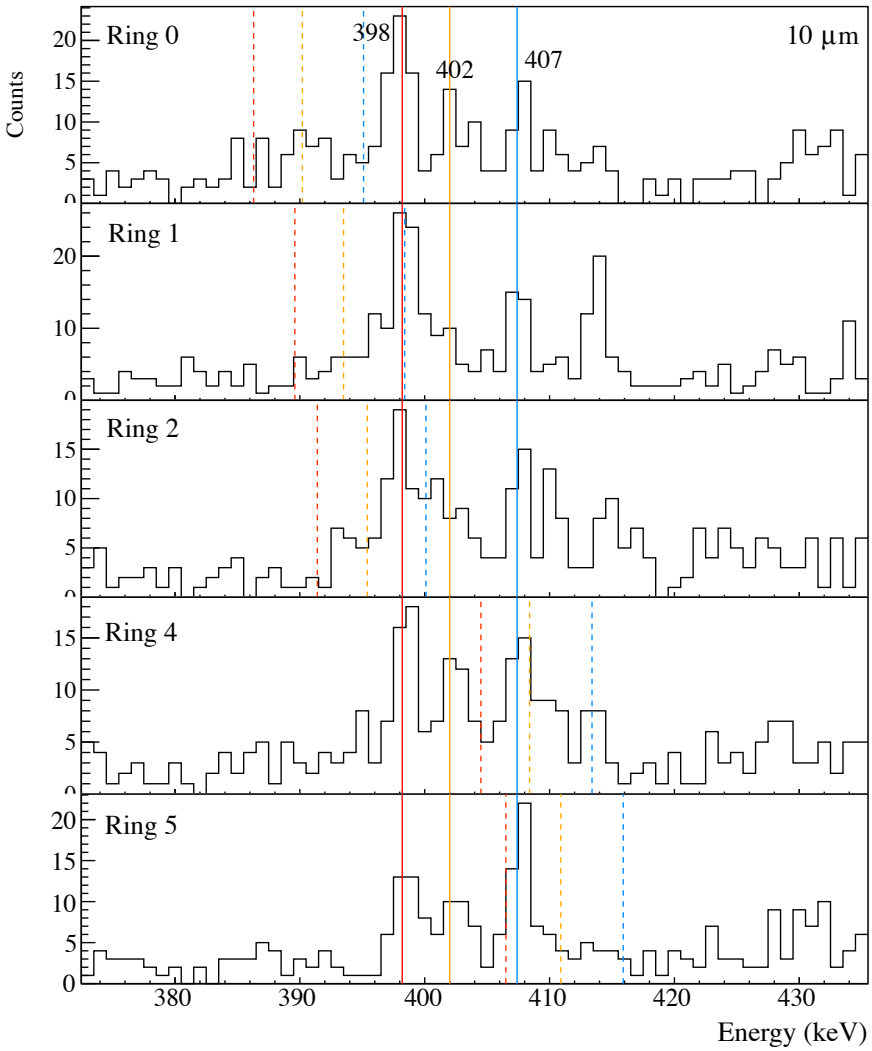


**Figure 5.10:** Partial gated $\gamma$-$\gamma$ coincidence spectra for DDCM analysis, measured by five ring combinations $\theta_i$ - $\theta_{AllDC}$ at 10 $\mu$m, obtained by gating on the Doppler shifted component ($B_s$) of the 286 keV $25/2^+ \rightarrow 23/2^+$ transition showing the overlap around the 407keV $23/2^+ \rightarrow 21/2^+$ transition in $^{105}$In. The solid and dashed blue vertical lines indicate the unshifted and shifted components, respectively.

The low statistics and overlap with the Doppler shifted and unshifted components of 398 keV $25/2^- \rightarrow 23/2^-$ transition and the 402 keV $31/2^- \rightarrow 29/2^-$ from the first negative parity band of $^{105}$In made the DDCM analysis inaccurate for most of the ring combinations, only $\theta_0$ - $\theta_{AllDC}$ was used in this work. The result $\tau$ = 2.9(1) ps from DDCM analysis is shown in Fig. 5.11.

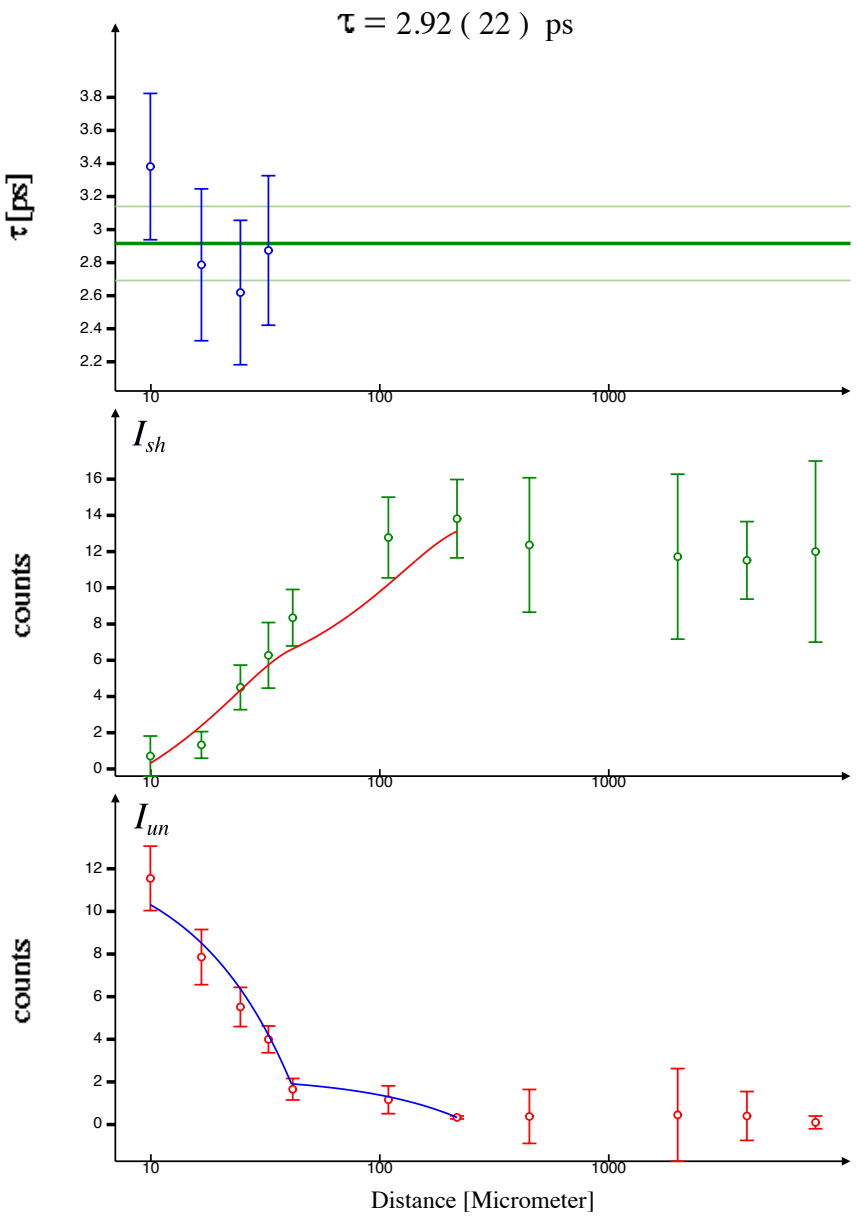


**Figure 5.11:** $\tau$-plot (Top) and intensities of the shifted $I_{sh}$ (middle) and unshifted $I_{un}$ (bottom) components of the 407keV $23/2^+ \rightarrow 21/2^+$ transition of $^{105}$In, measured at 152°, obtained via DDCM.

However, no peak of the depopulating 1248 keV transition could be observed in the gate on the 286 keV feeding transition due to the poor statistics.

### DCM

The DCM was used first for the 407 keV $23/2^+ \rightarrow 21/2^+$ transition by gating on the unshifted component of the strong low-lying 272 keV transitions, the statistics were greatly improved but the overlap problem was still observed for the depopulating 407 keV transition, as shown in Fig. 5.12.

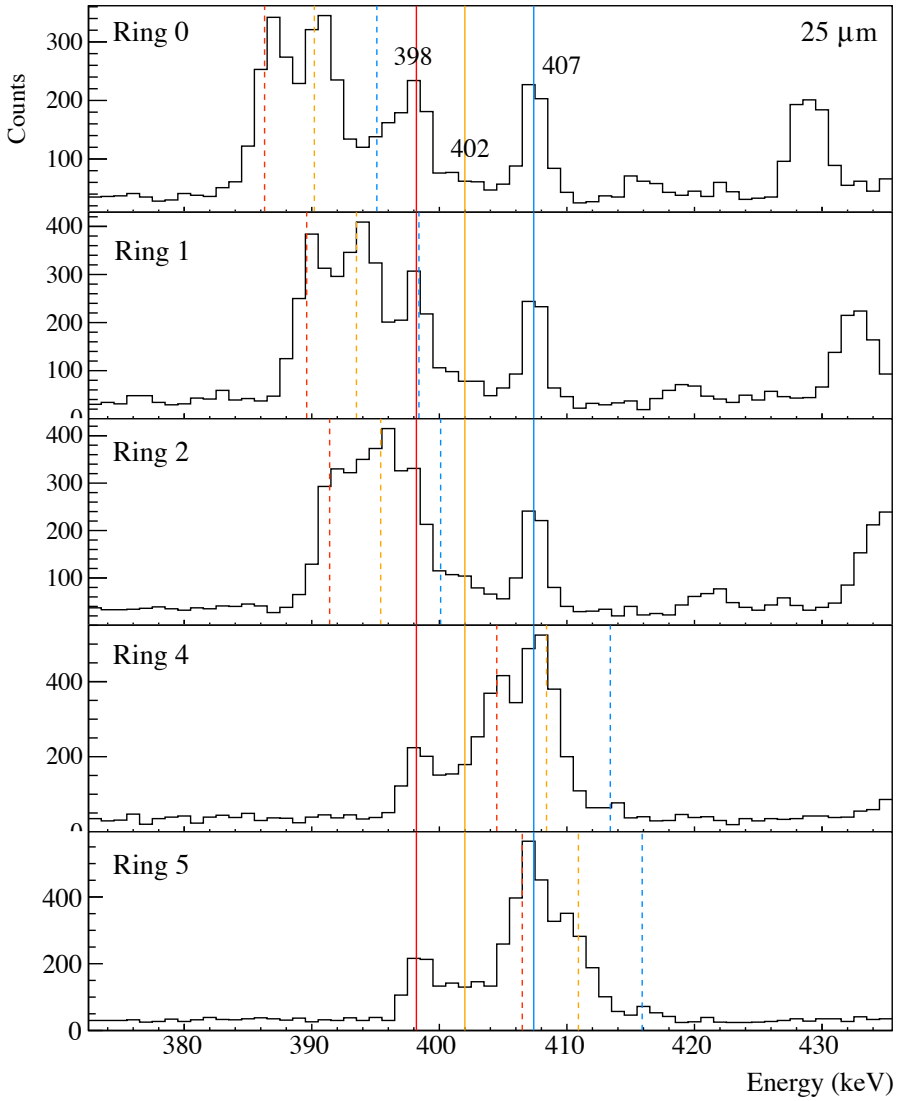


**Figure 5.12:** Partial gated $\gamma$-$\gamma$ coincidence spectra for DCM analysis, measured by five ring combinations $\theta_i$ - $\theta_{All}$ at 25 $\mu$m, obtained by gating on the unshifted component ($B_u$) of the 272 keV $19/2^+ \rightarrow 17/2^+$ transition showing the overlap around the 407keV $23/2^+ \rightarrow 21/2^+$ transition in $^{105}$In. The solid lines represent the unshifted peaks while the dashed lines for the shifted components.

In the case of the 1248 keV $23/2^+ \rightarrow 19/2^+$ transition with the same gate, no contamination was observed around the line of interest, as shown in Fig.5.13, which made the DCM analysis relatively operative. However, the lifetime of this state extracted by DCM, $\tau = 3.7(2)$ ps has large error due to the unknown sidefeeding time.

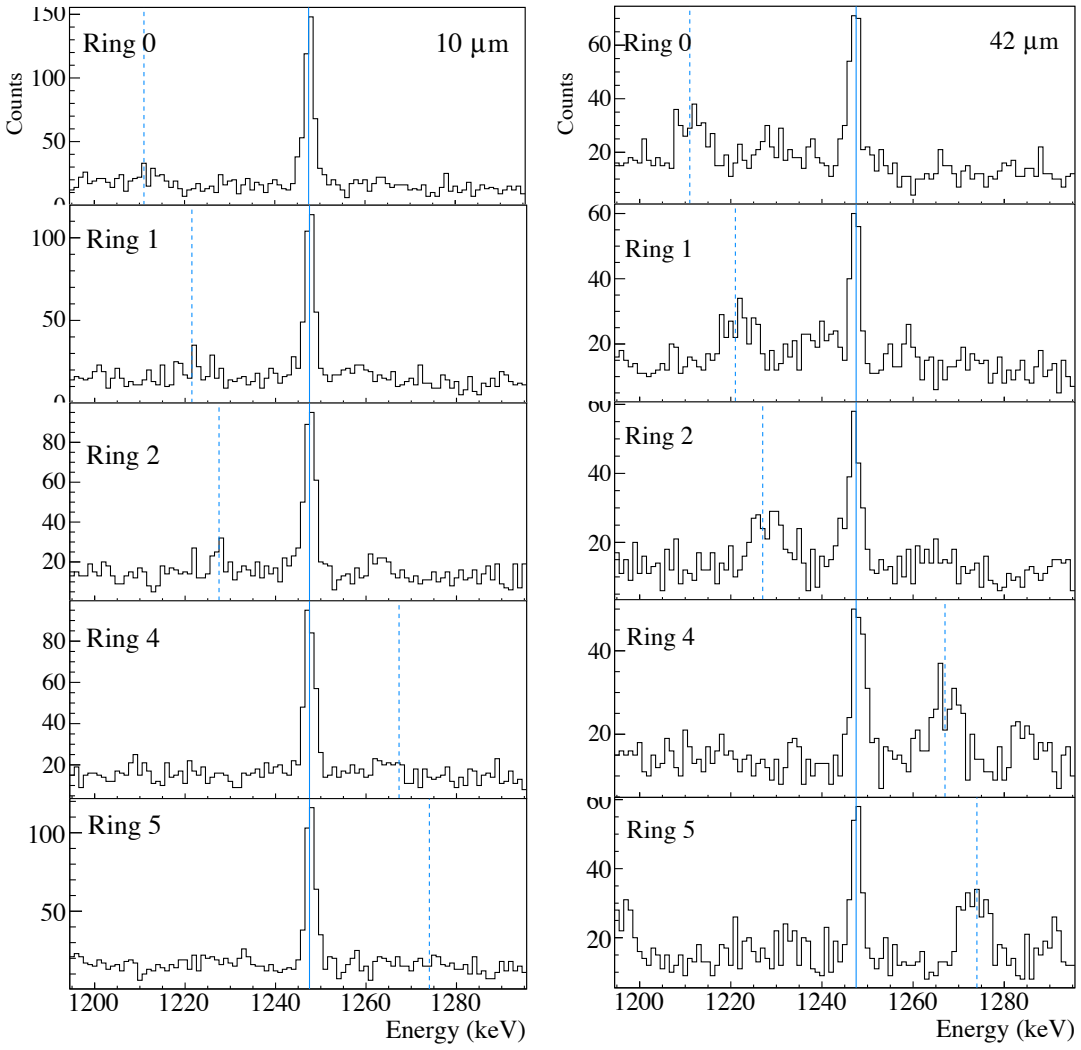


(a) DCM, at 10 $\mu$m

(b) DCM, at 25 $\mu$m

**Figure 5.13:** Partial gated $\gamma$-$\gamma$ coincidence spectra for DCM analysis for the 1248 keV $23/2^+ \rightarrow 19/2^+$ transition, obtained by gating on the unshifted component ($B_u$) of the 272 keV $19/2^+ \rightarrow 17/2^+$ transition , measured by five ring combinations $\theta_i$ - $\theta_{All}$ at 10 and 42 $\mu$m.

The $23/2^+$ state is a typical case with poor statistics, a number of contaminations and side-feeding. The lifetime extracted for the 407keV $23/2^+ \rightarrow 21/2^+$ transition from this work is $\tau = 2.9(2)$ ps, it is compatible with the value reported in literature 2.3(4) ps [9]. However, it should be noted that this value was extracted by only one ring combination.

Some main advantages and drawbacks of the DDCM and DCM methods are analytically illustruted:

- In the DDCM analysis, lifetimes can be measured with high precision in the dedicated plunger device, the side-feeding is perfectly eliminated by setting a gate at the sacrifice of data statistics. Contaminations that unfortunately occur frequently due to the large energy widths of the gates and the high line density observed in the reaction employed always cause severe limitation.
- For the DCM, the gating $\gamma$ ray can be chosen among all the strong transitions between low-lying states, it is therefore nearly always possible to find a spectrum without contaminations and with enough statistics [38]. However, side-feeding can result in large systematical uncertainties.

For these reasons we can say that DDCM and DCM are in a sense complementary. With the aim to validate the plunger technique, attention must be paid to the limitation factors mentioned above to choose the more appropriate one from the two different methods.

It should be aware that the measurement is not very reliable when these discussed limitations appears and the lifetime should be subject to further study to be sure of possible systematic errors, i.e. contamination, line shape effects, etc.

### 5.1.5 Lifetime of the $25/2^+$ state

The lifetime of this state was obtained by setting a gate on the shifted component of the 859 keV $29/2^+ \rightarrow 25/2^+$ transition (see Fig.1.1). The lifetime obtained is $\tau$ = 5.8(2) ps that is compatible with the value reported in literature of 5.9(2) ps. [8].

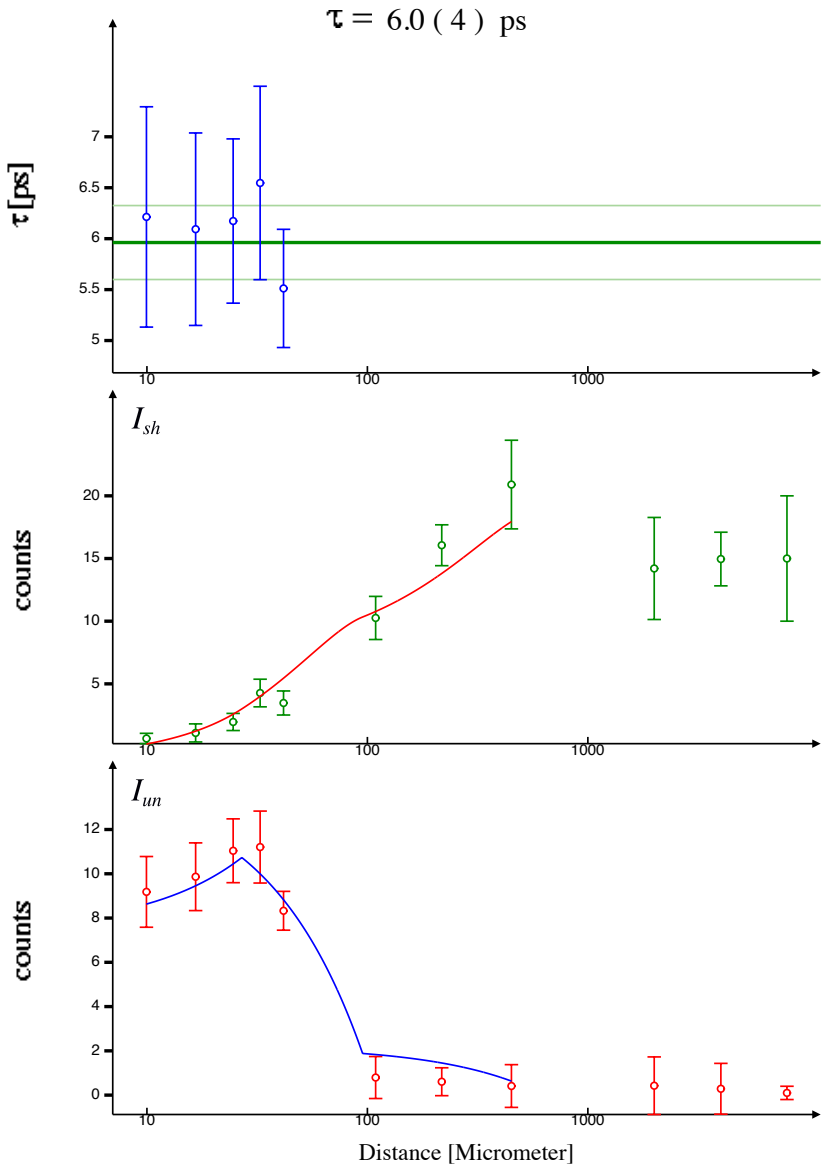


**Figure 5.14:** $\tau$-plot (Top) and intensities of the shifted $I_{sh}$ (middle) and unshifted $I_{un}$ (bottom) components of the 286 keV $25/2^+ \rightarrow 23/2^+$ transition of $^{105}$In, measured at 152°, obtained via DDCM.

| Ring combination | $\tau_{exp}$ [ps] |
|---|---|
| $\theta_0$ - $\theta_{AllDC}$ | 5.7(4) |
| $\theta_1$ - $\theta_{AllDC}$ | 5.7(3) |
| $\theta_2$ - $\theta_{AllDC}$ | 5.8(4) |
| $\theta_4$ - $\theta_{AllDC}$ | 6.0(4) |
| $\theta_5$ - $\theta_{AllDC}$ | 5.8(3) |
| Weighted Average | 5.8(2) |

**Table 5.6:** Table of lifetime values measured for the $25/2^+$ level, obtained via DDCM.

The results obtained for $^{105}$In are listed in Table 5.7 and representative for all investigated states. The extracted values from this work show good agreements with the previous measurement [8]) with reduced errors.

| $E_\gamma$ [keV] | $I_i^\pi \rightarrow I_f^\pi$ | $\tau_{exp}$ [ps] | literature$\tau$ [ps] |
|---|---|---|---|
| 485 | $17/2^+ \rightarrow 13/2^+$ | 605(5) | 600(40) |
| 272 | $19/2^+ \rightarrow 17/2^+$ | 3.90(7) | 3.76(18) |
| 840 | $21/2^+ \rightarrow 19/2^+$ | 0.92(5) | 0.75(15) |
| 407 | $23/2^+ \rightarrow 21/2^+$ | 2.9(2) | 2.3(4) |
| 286 | $25/2^+ \rightarrow 23/2^+$ | 5.8(2) | 5.9(2) |

**Table 5.7:** Table of measured lifetime values for the low-lying excited states in the GSB of $^{105}$In via DDCM, compared with results reported in literature. Literature values are taken from [8].

## 5.2 Lifetimes of the nucleus $^{104}$Cd

### 5.2.1 Lifetime of the $2^+$ state

The lifetime of the $2^+$ state of $^{104}$Cd was obtained by setting a gate on the shifted component of the 834 keV $4^+ \rightarrow 2^+$ transition (see Fig.1.2). Figure 5.15 shows the intensity curves of the Doppler shifted and unshifted components of the depopulating transition and the $\tau$-curve for the spectra recorded in ring combination $\theta_0$ - $\theta_{AllDC}$.

The lifetimes extracted from the five ring combinations are presented in Table 5.8. The average lifetime obtained for the $2^+$ state of $^{104}$Cd is $\tau = 8.9(2)$ ps, which agrees with the previous measurement 8.5(3) ps [42] and is more precise. The comparisons of the extracted values from this work and the value reported in literature is presented in Table 5.10.

| Ring combination | $\tau_{exp}$ [ps] |
|---|---|
| $\theta_0$ - $\theta_{AllDC}$ | 8.9(4) |
| $\theta_1$ - $\theta_{AllDC}$ | 9.2(5) |
| $\theta_2$ - $\theta_{AllDC}$ | 9.8(4) |
| $\theta_4$ - $\theta_{AllDC}$ | 8.4(3) |
| $\theta_5$ - $\theta_{AllDC}$ | 9.1(4) |
| Weighted Average | 8.9(2) |

**Table 5.8:** Table of lifetime values measured for the $2_1{}^+$ level of $^{104}$Cd, obtained via DDCM.

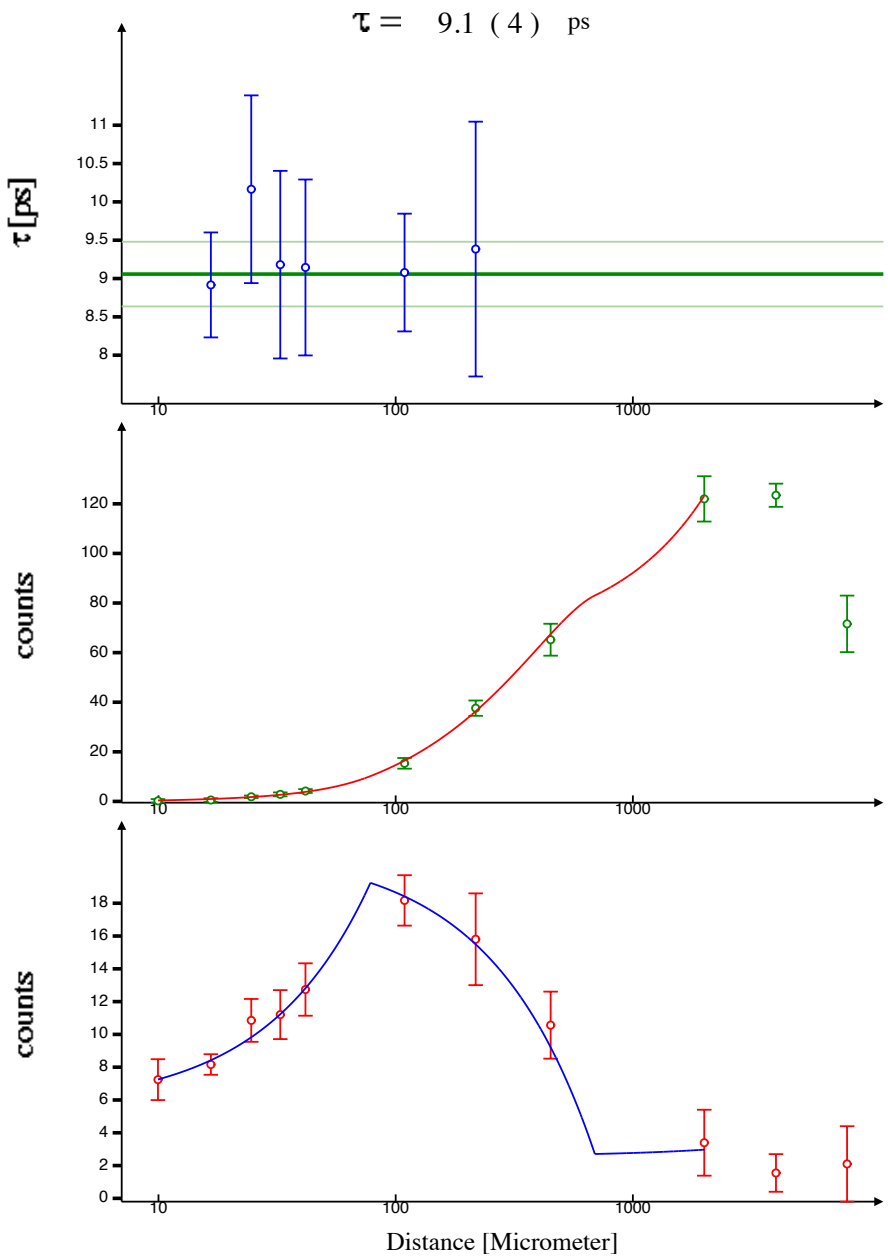


**Figure 5.15:** $\tau$-plot (Top) and intensities of the shifted $I_{sh}$ (middle) and unshifted $I_{un}$ (bottom) components of the 658 keV $2^+ \rightarrow 0^+$ transition of $^{104}$Cd, measured at 51°, obtained via DDCM.

### 5.2.2 Lifetime of the $4^+$ state

The lifetime of the $4^+$ state of $^{104}$Cd was obtained by setting a gate on the shifted component of the 878 keV $6^+ \rightarrow 4^+$ transition (see Fig.1.2).

Unfortunately, contaminations of $^{102}$Cd (see Fig.1.3) occurred due to the large energy widths of the gates and the high $\gamma$-ray density observed in the reaction employed in the gated spectra constructed from the five ring combinations $\theta_i$ - $\theta_{AllDC}$, as indicated in Fig. 5.16. The Doppler shifted component of 834 keV $4^+ \rightarrow 2^+$ transition in ring 2 overlaps with the unshifted component of the 822 keV $8^+ \rightarrow 6^+$ transition of $^{102}$Cd. For the ring combination $\theta_4$ - $\theta_{AllDC}$, the shifted component of the $4^+ \rightarrow 2^+$ transition at 847.2 keV overlaps with the unshifted component of the 847 keV $11 \rightarrow 9^-$ transition of $^{102}$Cd while the unshifted component overlaps with the shifted component of the 822 keV line of $^{102}$Cd.

The ring combinations $\theta_2$ - $\theta_{AllDC}$ and $\theta_4$ - $\theta_{AllDC}$ therefore could not be used in the lifetime analysis. Figure 5.9 shows the intensity curves of the Doppler shifted and unshifted components of the depopulating transition and the $\tau$-curve for the spectra recorded in ring combination $\theta_5$ - $\theta_{AllDC}$.

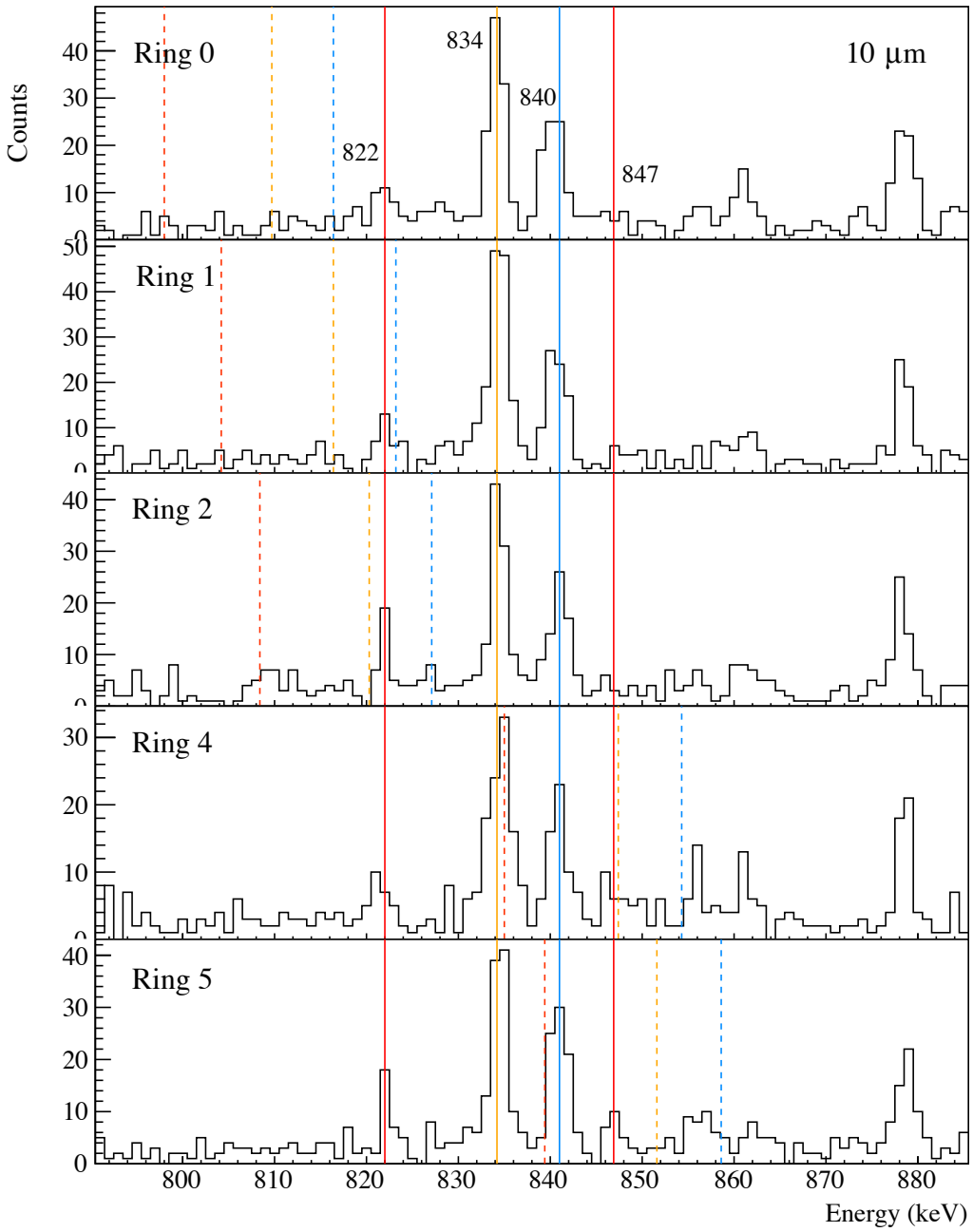


**Figure 5.16:** Check the contaminations around the shifted and unshifted components of the 834 keV $4^+ \rightarrow 2^+$ transition of $^{104}$Cd for the gated spectra measured at the five rings. The blue lines represent the contaminations from $^{105}$In and the red lines represent the contaminations from $^{102}$Cd. Solid and dash lines indicate the shifted and unshifted components of the contaminations, respectively.

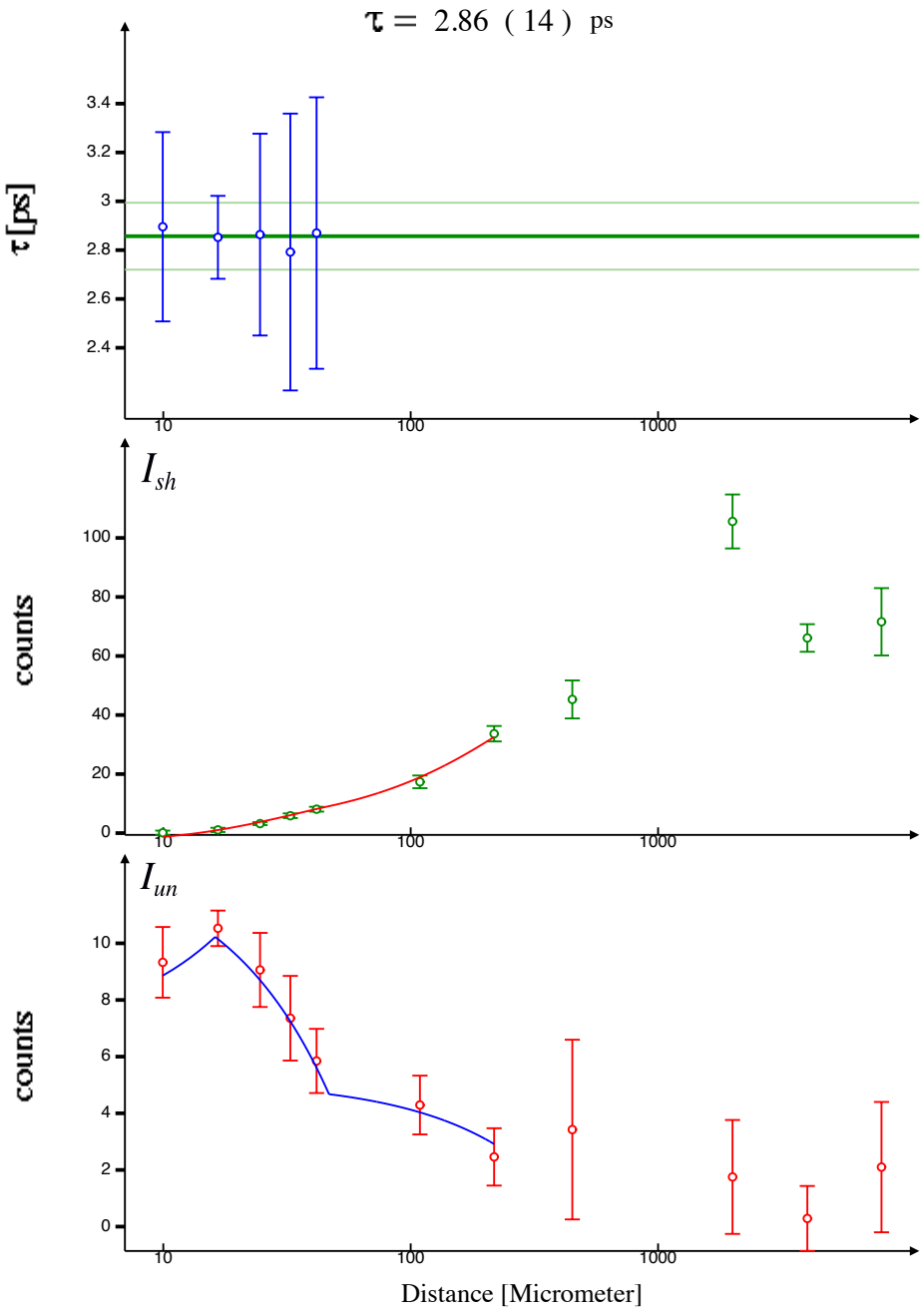


**Figure 5.17:** $\tau$-plot (Top) and intensities of the shifted $I_{sh}$ (middle) and unshifted $I_{un}$ (bottom) components of the 834 keV $4^+ \rightarrow 2^+$ transition of $^{104}$Cd, measured at 51°.

The lifetimes obtained for the $4^+$ state of $^{104}$Cd are listed in Table 5.17 together with a weighted average lifetime. The lifetime of this state was found to be larger than the previously measured value, which reflects the influence of the large gate width and low statistics to some extent.

| Ring combination | $\tau_{exp}$ [ps] |
|---|---|
| $\theta_0$ - $\theta_{AllDC}$ | 3.14(29) |
| $\theta_1$ - $\theta_{AllDC}$ | 2.75(12) |
| $\theta_5$ - $\theta_{AllDC}$ | 2.86(14) |
| Weighted Average | 2.8(1) |

**Table 5.9:** Table of lifetime values measured for the $4_1{}^+$ level, obtained via DDCM.

In Table 5.10 the results obtained for the two lowest-lying states of $^{104}$Cd from this work are summarised and compared to the previous experiment and the values reported in literature:

| $E_\gamma$ [keV] | $I_i^\pi \rightarrow I_f^\pi$ | $\tau_{exp}$ [ps] | literature $\tau$ [ps] |
|---|---|---|---|
| 658 | $2_1{}^+ \rightarrow 0_1{}^+$ | 8.9(2) | 9.1(30)[a] |
| | | | 8.5(3)[b] |
| 834 | $4_1{}^+ \rightarrow 2_1{}^+$ | 2.8(1) | $< 6.1$[a] |
| | | | 1.5(5)[b] |

**Table 5.10:** Table of measured lifetime values for the low-lying excited states in the GSB of $^{104}$Cd via DDCM, compared with results reported in literature. [a] from [7], [b] from [42].

### 5.2.3 Lifetime of the high-spin $11^+$ and $12^+$ states

The lifetime of the $11^+$ state of $^{104}$Cd was obtained by setting a gate on the shifted component of the 635 keV (12) $\rightarrow 11^+$ transition (see Fig.1.2). Due to the contaminations around the 717 keV depopulating transition, only three ring combinations were used for the DDCM analysis. Figure 5.9 shows the intensity curves of the Doppler shifted and unshifted components of the depopulating transition and the $\tau$-curve for the spectra recorded in ring combination $\theta_0$ - $\theta_{AllDC}$.

The lifetimes obtained for the $11^+$ state of $^{104}$Cd are listed in Table 5.12 together with a weighted average lifetime. The extracted value is in a good agreement with the previous experiment.

| Ring combination | $\tau_{exp}$ [ps] |
|---|---|
| $\theta_0$ - $\theta_{AllDC}$ | 76.2(5.0) |
| $\theta_4$ - $\theta_{AllDC}$ | 85.4(8.5) |
| $\theta_5$ - $\theta_{AllDC}$ | 79.9(5.7) |
| Weighted Average | 79.2(3.4) |

**Table 5.11:** Table of lifetime values measured for the $11^+$ level, obtained via DDCM.

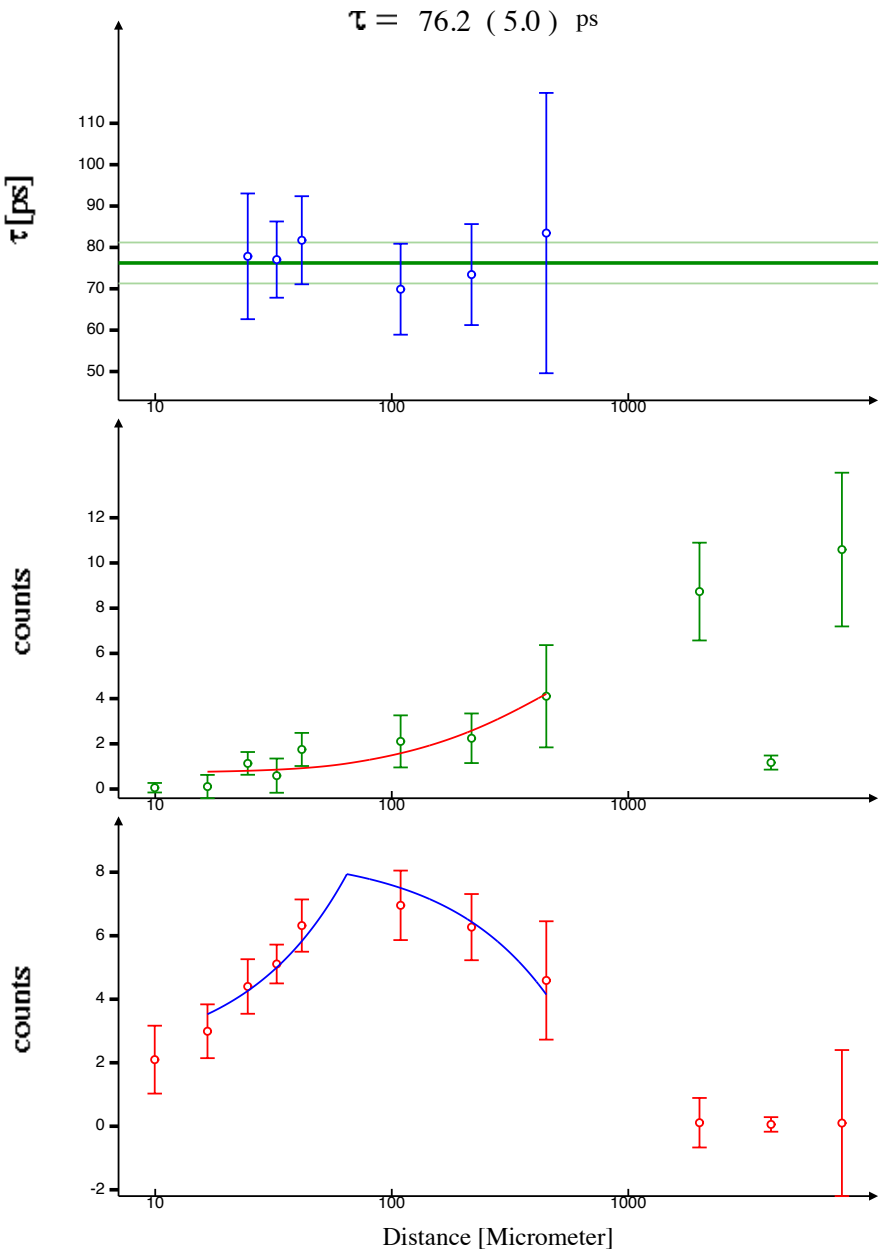


**Figure 5.18:** $\tau$-plot (Top) and intensities of the shifted $I_{sh}$ (middle) and unshifted $I_{un}$ (bottom) components of the 717 keV $11^+ \rightarrow 10^+$ transition of $^{104}$Cd, measured at 152°.

The lifetime of the $12^+$ state of $^{104}$Cd has been obtained for the first time by setting a gate on the shifted component of the 635 keV $13^+ \rightarrow 12^+$ transition (see Fig.1.2). Due to the contaminations around the 341 keV depopulating transition, only ring combinations $\theta_2$ - $\theta_{AllDC}$ and $\theta_4$ - $\theta_{AllDC}$ were used for the DDCM analysis. The

lifetimes obtained for the $12^+$ state of $^{104}$Cd are listed in Table 5.12 together with a weighted average lifetime.

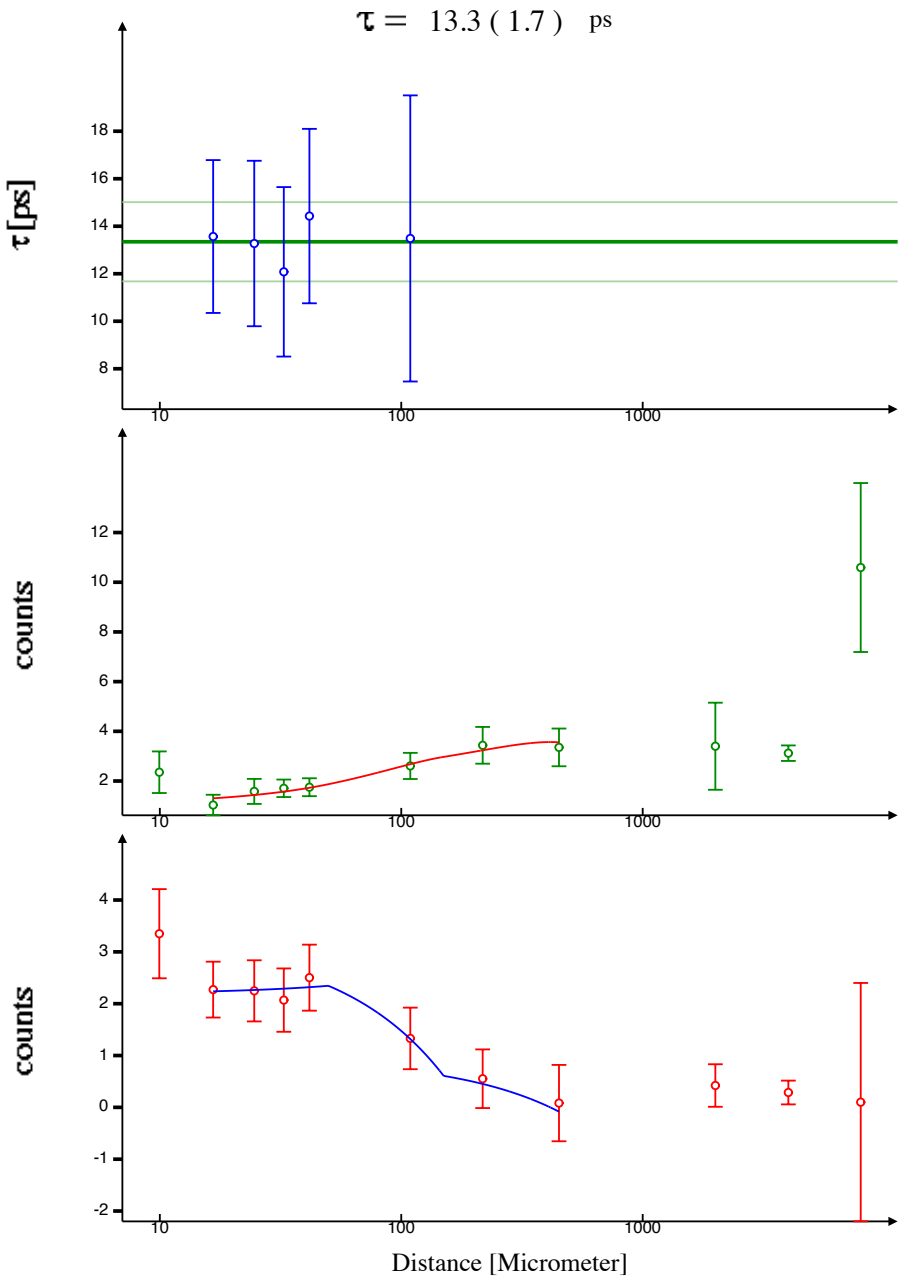


**Figure 5.19:** $\tau$-plot (Top) and intensities of the shifted $I_{sh}$ (middle) and unshifted $I_{un}$ (bottom) components of the 341 keV $12^+ \rightarrow 11^+$ transition of $^{104}$Cd, measured at 61°.

| Ring combination | $\tau_{exp}$ [ps] |
|---|---|
| $\theta_2$ - $\theta_{AllDC}$ | 13.3(1.7) |
| $\theta_4$ - $\theta_{AllDC}$ | 11.4(1.4) |
| Weighted Average | 12.2(1.1) |

**Table 5.12:** Table of lifetime values measured for the $12^+$ level, obtained via DDCM.

In Table 5.13 the results obtained for the two high-spin states of $^{104}$Cd are summarised and compared to the literature adopted values:

| $E_\gamma$ [keV] | $I_i^\pi \rightarrow I_f^\pi$ | $\tau_{exp}[ps]$ | literature $\tau$ [ps] |
|---|---|---|---|
| 717 | $11^+ \rightarrow 10^+$ | 79(3) | 79(6)$^a$ |
| 341 | $12^+ \rightarrow 11^+$ | 12(1) | |

**Table 5.13:** Table of measured lifetime values for $^{104}$Cd via DDCM, compared with results reported in literature. $^a$ from [7].

# Chapter 6

# Theoretical Interpretation

In the previous chapter, lifetime measurements of excited states in the neutron-deficient N = 56 isotones $^{105}$In and $^{104}$Cd have been presented. As outlined in Chapter 2, experimental values of the reduced transition probabilities, can be subsequently extracted. The lifetime measurements for excited states in the yrast bands of the neutron-deficient N = 56 isotones $^{105}$In and $^{104}$Cd performed in this work and the important probes of nuclear structure, hence provide further opportunities to test the model predictions. To contextualize the results, comparisons of the results from this work and the theoretical calculations are presented. Furthermore, the systematics of the relevant spectroscopy and electromagnetic transition properties across the In and Cd isotopes around $^{100}$Sn are discussed.

## 6.1 The robust Z = 50 shell closure

Isotopes in the neighborhood of the doubly-magic Z = N = 50 core $^{100}$Sn obviously are ideal candidates for testing the nuclear shell model and their reduced transition probabilities are the important probes of nuclear structure. The comparison of the experimental $B(E2)$ values from this work and the shell model calculations are listed in Table 6.1.

| | $E_\gamma$ | $I_i^\pi \rightarrow I_f^\pi$ | $\tau_{exp}$ | $B(E2)_{exp}$ | $B(E2)_{calc}$ |
|---|---|---|---|---|---|
| | $[keV]$ | | [ps] | $[e^2fm^4]$ | $[e^2fm^4]$ |
| $^{104}$Cd | 658 | $2_1{}^+ \rightarrow 0_1{}^+$ | 8.9(2) | 744(17) | 749[a] |
| | 834 | $4_1{}^+ \rightarrow 2_1{}^+$ | 3.73(7) | 724(26) | 1073[a] |
| $^{105}$In | 485 | $17/2^+ \rightarrow 13/2^+$ | 605(5) | 1.71(2) | 1.45[b] |

**Table 6.1:** Table with measured lifetime values, experimental and calculated $B(E2)$ values for the low-lying excited states in the GSBs of $^{104}$Cd and $^{105}$In. [a] from [17], [b] from [9].

The small $E2$ strengths confirm the sphericity of the doubly-magic Z = N = 50 core $^{100}$Sn. It is instructive to look to the even-even cadmium nuclei in the Cd isotopic chain, especially the neighbouring $^{102}$Cd and $^{106}$Cd.

The reduced transition probability $B(E2; 0^+ \rightarrow 2^+)$ of $^{104}$Cd is significantly larger than earlier results for $^{102}$Cd and lower than values for $^{106}$Cd [17]. The result is well reproduced by shell model predictions and therefore indicates a robust Z = 50 shell closure.

Good agreement of measured and calculated $B(E2)$ values reveals the effectiveness of the shell model for the low-lying excited states.

## 6.2 Collective versus Magnetic Rotation in the A $\sim$ 100 mass region

The angular momentum in a magnetic dipole band is generated either through collective rotation around a principal axis (PAR) or by gradual alignment of the angular momenta of the valence neutrons and protons around an axis which is tilted with respect to the rotational axis (TAR also know as Magnetic Rotation). The $B(M1)$ value is an important probe to distinguish these two mechanisms. In case of collective rotation, characteristic staggering can be observed in both

$I \rightarrow I$ 1 transition energies and magnetic transition strengths, while in the case of Magnetic Rotation, $I \rightarrow I$ 1 transition energies and magnetic transition strengths show a smooth increase and decrease with increasing angular momentum, respectively.

The comparison of the experimental $B(M1)$ values from this work and the shell model calculations is in Table 6.2.

| | $E_\gamma$ | $I_i^\pi \rightarrow I_f^\pi$ | $\tau_{exp}$ | $B(M1)_{exp}$ | $B(M1)_{calc}$ |
|---|---|---|---|---|---|
| | $[keV]$ | | [ps] | [m$\mu_N{}^2$] | [m$\mu_N{}^2$] |
| $^{105}$In | 272 | $19/2^+ \rightarrow 17/2^+$ | 3.90(7) | 395(7) | $223^b$ |
| | 840 | $21/2^+ \rightarrow 19/2^+$ | 0.92(5) | 55(3) | $1.5^b$ |
| | 407 | $23/2^+ \rightarrow 21/2^+$ | 2.9(1) | 95(5) | $68^b$ |
| | 286 | $25/2^+ \rightarrow 23/2^+$ | 5.8(2) | 227(7) | $108^b$ |
| $^{104}$Cd | 717 | $11^+ \rightarrow 10^+$ | 79(3) | 1.07(4) | |
| | 341 | $12^+ \rightarrow 11^+$ | 12(1)* | 65(5) | |

**Table 6.2:** Table with measured lifetime values, experimental and calculated $B(M1)$ values. $^b$ from [9]. The lifetime of the $12^+$ state of $^{104}$Cd was measured for the first time.

The $B(M1)$ strengths measured for the low-lying states in the ground state band of $^{105}$In are shown to be compatible with the shell model predictions, however they do not regularly decrease with increasing rotational frequency but are rather constant, which suggests that this $M1$ bands arise from the collective rotation of a weakly oblate shape. It is noticeable that the $B(M1)$ values of the high-lying $\Delta I = 1$ band of $^{105}$In fail to agree with shell-model calculations from the previous work [9]. These observations indicate that there are other possible excitation mechanisms responsible for the generation of spin in the high-lying $M1$ sequence. One possible mode of excitation is the "shears mechanism" (or magnetic rotation), as indicated in Chapter 2. One consequence of the shears mechanism describe that one should observe decreasing $B(M1)$ values along a band, because increasing the

angular momentum by closing of the blades reduces the transversal component of the magnetic moment.

The dipole transitions along with very weak crossover $E2$ transitions were observed in $^{104}$Cd, which can be a possible candidate of magnetic rotation band, however, insufficient intensity to perform a lifetime analysis for higher spin states. The extracted experimental $B(M1)$ values do not regularly decrease with increasing rotational frequency, corresponding to a fluctuation in the shears angle due to the relatively high contribution from collective motion.

In contrast to the Pb isotopes, where the shears mechanism is the main source for the generation of angular momentum, in the In and Cd isotopes a substantial fraction of the angular momentum is generated by the normal parity neutrons. The shears mechanism is less effective for the light In and Cd isotopes (only three orbitals $v(d_{5/2}, g_{7/2}, h_{11/2})$ are involved instead of four orbitals with larger $j$-values in the case of the Pb isotopes).

The $^{105}$In and $^{104}$Cd are an example that the concept of magnetic rotation is more general than the shears bands model for the Pb isotopes where it originated from. The mechanisms of generating the angular momentum are more diverse. Our result indicates that the shear mechanism and conventional rotation (for well-deformed nuclei) remain unable to describe the magnetic rotation in exotic neutron-deficient isotopes approaching N = Z = 50.

# Chapter 7

# Conclusions and Further Perspectives

In the present work, lifetimes of excited states of $^{105}$In and $^{104}$Cd have been measured with the coincidence Recoil Distance Doppler Shift (RDDS) technique. The experiment was conducted by impinging a 180 MeV $^{50}$Cr beam on a $^{58}$Ni target to populate the neutron-deficient $^{100}$Sn region on the nuclear chart via a fusion-evaporation reaction. A highly selective setup composed of the $\gamma$-ray spectrometer GALILEO coupled with the charged particles detector array EUCLIDES and a dedicated plunger device for GALILEO was employed.

Yrast states $17/2^+$ up to $25/2^+$ in the GSB of $^{105}$In and $2^+$, $4^+$ in the GSB of $^{104}$Cd have been remeasured and compared with the previous experiments with the aim to validate the experimental technique. In addition, two high spin states $11^+$ and $12^+$ in $^{104}$Cd have been studied. The lifetime of the $12^+$ state has been measured for the first time.

**The plunger technique validation**

In this dissertation, the DDCM and DCM technique have been discussed and compared for the lifetime investigation. Most of the extracted lifetimes are consistent with previous measurements, while the uncertainties could be reduced

significantly using the DDCM analysis.

However, limitation factors for the DDCM and DCM have also been analytically illustrated through the analysis of the $21/2^+$, $23/2^+$ states in $^{105}$In. The lifetime of the $21/2^+$ state in $^{105}$In was found to be larger than the previously measured value due to the presence of a contaminant line from higher-lying level falling under the gate in ring 1, and therefore causes extra unshifted components for the transition of interest in the accumulated spectra of the sum of the five GALILEO ring combinations. While for the $23/2^+$ state, very low statistics of the depopulating 407 keV transition and a number of contaminants around the $\gamma$ line of interest made the DDCM impossible for most of the ring combinations. In the DCM analysis, the statistics was significantly improved by gating on a strong low-lying transition, but systematic uncertainties due to the unknown side-feeding time arose. However, the side-feeding is perfectly eliminated by setting a gate at the sacrifice of data statistics in the DDCM analysis.

Another problem has been indicated via the DDCM analysis of the $4^+$ state of $^{104}$Cd. Contaminations from $^{102}$Cd and $^{105}$In occurred around the transition of interest of $^{104}$Cd due to the large energy widths of the gates and the high $\gamma$-ray density populated by fusion-evaporation reaction. Therefore, considering the width of the gate used in the analysis, there needs to be a compromise between high data statistics and peaks without contaminations. It is suggested to be 3 keV since the average energy resolution for the full GALILEO array is $\sim$2.4 keV.

In summary, I would conclude that the first aim of this project, to validate the coincidence plunger technique has been met. However, attention must be paid to the limitation factors, i.e. the low statistics of the data, the contaminations around the populating or depopulating $\gamma$ rays of the state of interest, the width of the gate and the side-feeding effect. In the plunger data analysis, the DDCM and DCM are in a certain sense complementary and one should choose the more appropriate one according to the actual situation. In practice, the DDCM is good for the low-lying states in the GSB while the DCM has a great advantage of

statistics for the very weak high-lying states.

**The electromagnetic strengths investigation**

Since the measured lifetimes enabled the assessments of the multipolarities of the $\gamma$ rays depopulating the states of interest. Information on electromagnetic transition strengths $B(E2)$ and $B(M1)$, which are sensitive probes of nuclear structure, were deduced for the $\gamma$-ray transitions.

Good agreement of measured and calculated $B(E2)$ values of the low-lying states reveals the effectiveness of the shell model at low spin. Moreover, the reduced transition probability $B(E2; 0^+ \rightarrow 2^+)$ of $^{104}$Cd determined from this work is significantly larger than earlier results for $^{102}$Cd and lower than values for $^{106}$Cd [17]. The result favored the generalized seniority scheme which predicts a parabolic behaviour of the $B(E2; 0^+ \rightarrow 2^+)$ values along the Cd chain and therefore indicates a robust Z = 50 shell closure.

The $B(M1)$ values have been deduced for the excited states in the GSB of $^{105}$In and the rotational band built upon the $I^\pi = 6^+$ state (band 1) of $^{104}$Cd. It has been demonstrated through the characteristic staggering of the transition energies and the $B(M1)$ values that the low spin states in the GSB of $^{105}$In originates due to collective rotation.

However, the band 1 of $^{104}$Cd has observed to be characterized by strong $M1$ transitions and very weak $E2$ crossover transitions. In order to assess the possibility of magnetic rotation as an alternative scenario for explaining the observed band structure, two high spin states $11^+$ and $12^+$ of $^{104}$Cd were investigated. However, the $B(M1)$ values failed to show a decrease with increasing angular momentum.

**Further Perspectives**

The coincidence plunger technique validated in the present work is a powerful tool to obtain lifetimes in the range $10^{-9} - 10^{-12}$ s. It is worthwhile to stress that for the transitions with low statistics, contaminations around either the directly populating or depopulating transitions or side-feeding, the lifetime measurement is not very reliable and the lifetime should be subject to further study to be sure of possible systematic errors. In general, investigation should be started from the contaminations analysis, as discussed in Chapter 5.

The coupling of the GALILEO-EUCLIDES-Plunger setup with other ancillary detectors, such as the neutron detectors (Neutron Wall, NEDA) will provide higher selectivity. As a result, for example, in the gated spectra of the $4^+$ state of $^{104}$Cd, contaminations from the $^{102}$Cd and $^{105}$In can be totally eliminated.

For the next step, another product $^{105}$Sn populated in this experiment can be investigated with the plunger technique. The $B(E2)$ value can be deduced to test the robustness of the proton shell closure approaching N = 50. With the $B(M1)$ value, it is possible to investigate the magnetic rotation in $^{105}$Sn.

In the case of the $M1$ band in $^{104}$Cd, further studies are expected to confirm whether the tilted axis cranking satisfactorily explain the properties of the band or the shears mechanism and collective rotation interplay in band 1 of $^{104}$Cd.

With more lifetimes in the light Sn, In and Cd isotopes become available, the door will be opened for a comprehensive comparison of transition probabilities in nuclei and to an improved understanding of the shell-closure evolution in the $^{100}$Sn region.

# Bibliography


[1] R. Machleidt. "The high-precision, charge-dependent Bonn nucleon-nucleon potential (CD-Bonn)". In: *Physical Review C* 63 (June 2000). DOI: 10.1103/PhysRevC.63.024001 (cit. on p. 1).

[2] M. Siciliano, Jose Javier Valiente Dobon, and Alain Goasduff. "Nuclear structure of the semi-magic tin isotopes close to $^{100}$Sn: lifetime measurements of low-lying states in $^{106}$Sn and $^{108}$Sn". In: 2017 (cit. on p. 1).

[3] G. Pasqualato et al. *Lifetime measurements in $^{105}$Sn: the puzzle of B(E2) and B(M1) strengths in Sn isotopes*. DOI: 10.1051/epjconf/201922301048 (cit. on pp. 1, 2, 25).

[4] D. Kast et al. "Lifetime study of high-spin states in $^{104,105}$In". In: *Eur. Phys. J. A* 3.2 (1998), pp. 115–128. DOI: 10.1007/s100500050157 (cit. on pp. 2, 4, 46).

[5] Nele Boelaert. "Master thesis". In: *Ghent University* (2006) (cit. on pp. 2, 7).

[6] D. Frenne. *Nuclear Data Sheets for A = 102*. Vol. 110. 8. 2009, pp. 1745–1915. DOI: https://doi.org/10.1016/j.nds.2009.06.002 (cit. on pp. 2, 6).

[7] Jean Blachot. *Nuclear Data Sheets for A = 104*. 2007. DOI: https://doi.org/10.1016/j.nds.2007.09.001 (cit. on pp. 2, 5, 76, 80).

[8] S. Lalkovski, J. Timar, and Z. Elekes. “Nuclear Data Sheets for A=105”. In: vol. 161-162. 2019, pp. 1–353. DOI: https://doi.org/10.1016/j.nds.2019.11.001 (cit. on pp. 2, 56, 58, 61, 63, 69, 70).

[9] D. Kast et al. *Lifetime study of high-spin states in* $^{104,105}$*In*. 1998, pp. 115–128 (cit. on pp. 4, 7, 8, 10, 44, 63, 68, 82, 83).

[10] R. Clark and A. Macchiavelli. “The Shears Mechanism in Nuclei”. In: *Annual Review of Nuclear and Particle Science - ANNU REV NUCL PAR SCI* 50 (Jan. 2000), pp. 1–36 (cit. on pp. 3, 10, 11).

[11] Rejmund M. Maier K. “Shell model interaction between proton holes and between proton holes and neutron particles around $^{208}$Pb”. In: *European Physical Journal A 14* (2002), p. 349. DOI: https://doi.org/10.1140/epja/i2002-10006-0 (cit. on p. 7).

[12] J. Kownacki et al. “High-spin studies of the neutron deficient nuclei $^{103}$In, $^{105}$In, $^{107}$In, and $^{109}$In”. In: *Nuclear Physics A* 627.2 (1997), pp. 239–258. DOI: https://doi.org/10.1016/S0375-9474(97)00479-X (cit. on p. 7).

[13] N.S. Kelsall et al. “Evidence for shears bands in $^{108}$ Cd”. In: *Physical Review C* 61.1 (1999), p. 011301 (cit. on p. 8).

[14] D. Negi et al. “High spin spectroscopy and shears mechanism in$^{107}$*In*”. In: *Phys. Rev. C* 81 (May 2010). DOI: 10.1103/PhysRevC.81.054322 (cit. on p. 8).

[15] Kris L.G. Heyde. “The nuclear shell model”. In: *The Nuclear Shell Model*. Springer, 1994, pp. 58–154 (cit. on pp. 8, 9).

[16] D. Seweryniak et al. “In-beam study of $^{102}$ In, $^{104}$In and $^{106}$In”. In: *Nucl. Phys. A* 589 (1995), pp. 175–200. DOI: 10.1016/0375-9474(95)00060-E (cit. on p. 10).

[17] N. Boelaert et al. “Shell model description of the low-lying states of the neutron deficient Cd isotopes”. In: *Phys. Rev. C* 75 (1 Jan. 2007), p. 014316. DOI: 10.1103/PhysRevC.75.014316 (cit. on pp. 10, 82, 87).

[18] G. de Angelis et al. "Collective excitations in the vicinity of N=Z". In: *Nuclear Physics A* 654.1, Supplement 1 (1999), pp. 659c–662c. DOI: https://doi.org/10.1016/S0375-9474(00)88521-8 (cit. on p. 11).

[19] Jouni Suhonen. *From Nucleons to Nucleus. Concepts of Microscopic Nuclear Theory*. Springer-Verlag Berlin Heidelberg, 2007. DOI: 10.1007/978-3-540-48861-3 (cit. on pp. 12, 14).

[20] A. Bohr and B.R. Mottelson. *Nuclear structure. Volume II. Nuclear deformations*. Jan. 1975 (cit. on pp. 14, 16).

[21] P. Petkov et al. "In-band M1 and E2 transition rates and collective structures in $^{128}$Ba". In: *Nuclear Physics A* 640.3 (1998), pp. 293–321. DOI: https://doi.org/10.1016/S0375-9474(98)00429-1 (cit. on p. 16).

[22] Forster J.S. Alexander T.K. *Lifetime measurements of excited nuclear levels by Doppler-shift methods*. 1979, pp. 197–331 (cit. on p. 18).

[23] P.J. Nolan and J.F. Sharpey-Schafer. *The measurement of the lifetimes of excited nuclear states*. Jan. 1979. DOI: 10.1088/0034-4885/42/1/001 (cit. on pp. 19, 32).

[24] J.J. Valiente Dobon D. Mengoni F. Recchia. "The GALILEO Array at LNL". In: (2013). URL: http://www.lnl.infn.it/~annrep/read_ar/2013/contributions/pdfs/074_C_118_C113.pdf (cit. on pp. 20, 23, 24, 26, 28).

[25] C. Müller-Gatermann et al. "A new dedicated plunger device for the GALILEO $\gamma$-ray detector array". In: *Nuclear Instruments and Methods in Physics Research Section A* 920 (2019), pp. 95–99. DOI: https://doi.org/10.1016/j.nima.2018.12.077 (cit. on pp. 20, 27, 28).

[26] D. Testov et al. *High Resolution $\gamma$-Ray Spectroscopy Using GALILEO Array*. DOI: 10.1142/9789811209451_0068 (cit. on pp. 20, 26, 27).

[27] M. Siciliano. *Shape Coexistence in the Neutron-Deficient Nucleus $^{194}$Po*. DOI: 10.13140/RG.2.1.1885.1365 (cit. on p. 22).

[28] *The colourful nuclide chart.* URL: http://people.physics.anu.edu.au/%20ecs103/chart/ (cit. on p. 23).

[29] Glenn F. Knoll. *Radiation Detection and Measurement.* Don Fowley, 2010 (cit. on p. 25).

[30] I. Zanon. *Master thesis (2018).* URL: http://tesi.cab.unipd.it/61172/1/Zanon%20Irene%20tesi.pdf (cit. on pp. 25, 26).

[31] D. Testov E. Tronchin M. Siciliano. *Tuning of the BGO anti-Compton shield in the GALILEO array.* URL: https://www.lnl.infn.it/~annrep/read_ar/2014/contributions/pdfs/093_C_126_C121.pdf (cit. on p. 25).

[32] J. Gutleber et al. "Towards a homogeneous architecture for high-energy physics data acquisition systems". In: *Computer Physics Communications* 153.2 (2003), pp. 155–163. DOI: https://doi.org/10.1016/S0010-4655(03)00161-9 (cit. on p. 26).

[33] S.D. Bakes. "Lifetime Measurements Far From Stability: the Systematics and Octupole Deformation of $^{110}$Te". In: (2019) (cit. on pp. 28, 29, 33, 53).

[34] A. Candiello. "Nuclear Structure of 33S using the GALILEO $\gamma$-ray spectrometer". In: (2019) (cit. on p. 29).

[35] A. Goasduff et al. *A New Dedicated Plunger Device for the GALILEO $\gamma$-ray array.* DOI: 10.1016/j.nima.2018.12.077 (cit. on pp. 29, 31).

[36] A. Dewald et al. *Developing the Recoil Distance Doppler-Shift technique towards a versatile tool for lifetime measurements of excited nuclear states.* Vol. 67. 3. 2012, pp. 786–839. DOI: https://doi.org/10.1016/j.ppnp.2012.03.003 (cit. on pp. 36, 40–43, 45).

[37] P. Petkov. "Errors arising from nuclear hyperfine interactions on lifetimes determined by the recoil distance Doppler shift method". In: *Nuclear Instruments and Methods in Physics Research Section A* 349.1 (1994), pp. 289–291. DOI: https://doi.org/10.1016/0168-9002(94)90636-X (cit. on p. 43).

[38] G.A. Müller et al. “High-spin structure and electromagnetic transition strengths in $^{104}$ Cd”. In: *Physical Review C* 64.1 (2001), p. 014305 (cit. on pp. 43, 44, 68).

[39] B. Saha. *Napatau or Tk-Lifetime-Analysis* (cit. on pp. 48, 53).

[40] R. Brun and F. Rademakers. “ROOT — An object oriented data analysis framework”. In: *Nuclear Instruments and Methods in Physics Research Section A* 389.1 (1997). New Computing Techniques in Physics Research V, pp. 81–86. DOI: https://doi.org/10.1016/S0168-9002(97)00048-X (cit. on pp. 49, 50).

[41] L.P. Gaffney et al. “Shape coexistence in neutron-deficient Hg isotopes studied via lifetime measurements in $^{184,186}$Hg and two-state mixing calculations”. In: *Phys. Rev. C* 89 (2 Feb. 2014), p. 024307. DOI: 10.1103/PhysRevC.89.024307 (cit. on p. 53).

[42] N. Boelaert et al. “Low-spin electromagnetic transition probabilities in $^{102,104}$Cd”. In: *Phys. Rev. C* 75 (5 May 2007), p. 054311. DOI: 10.1103/PhysRevC.75.054311 (cit. on pp. 71, 76).